UiO : Department of Informatics
University of Oslo

Prototyping a measurement device for evaluating the performance of cross-country skis

Investigation of pressure-distribution

Petter Kristiansen

Master's Thesis, Autumn 2019

Abstract

Cross-country skiing is by many used for recreational purposes. However, cross-country skiing is also a highly competitive Olympic sport. For competitive cross-country skiing, the performance of the skis is of utmost importance. Therefore, much time and energy are spent on tuning and analyzing the mechanical properties of the skis to increase every chance of victory in competitive skiing.

In this thesis, we investigate the pressure distribution from the cross-country skis to the snow. A prototype of a complete mechanical system is developed, using multiple cheap commercially available pressure-sensitive film sensors to measure the force or pressure underneath the ski. We describe the full process of designing a prototype to measure the pressure distribution. From the design of the mechanical system, how we apply a load mimicking the skier to classical cross-country skis, to the analysis of the sensor characteristics and circuit behavior.

It was found that the mechanical property pressure distribution could be used to find skis suitable for different weather and snow conditions. This was done by investigating the pressure distribution from two pairs of skis. Cross-country skis suitable for wet snow and warm weather conditions were assumed to have equal pressure zones for both sides of the camber pocket of the ski, with the peak load close to the camber pocket. Also, a shorter contact area for the front section of the ski contributed to the assumptions for warm skis. Cold skis were characterized as more extended contact areas for the front section and a higher peak load in the back section. The calibrations of the sensors had a significant impact on the measurement quality. Due to the combined error from the calibrations and microcontroller unit used, the measurement results proved too inaccurate to draw reliable conclusions on weather classification of skis and twisting in the structure of the ski.

Contents

List of Figures

List of Tables

Acknowledgement

This master thesis marks the end of my master's degree study in Digital Signal Processing at the University of Oslo. This also marks the beginning of a new era with endless possibilities. I would like to thank everyone who made this possible.

I would like to express my deepest gratitude to my supervisors Ole Marius Hoel Rindal and Andreas Austeng. They have gone above and beyond to make this master thesis exciting. During difficult and frustrating times, they have always kept their door open and put time aside to assist in every possible way. Thank you for all your invaluable help, guidance, and patience during this process.

A big thanks to the talented personnel at the Institute of Physics. Jonas Ringnes from the Instrument Laboratory and David Michael Bang-Hauge from Electronics Laboratory which always replied to my questions and assisted during the manufacturing stage with eagerness.

I would finally like to show my deepest gratitude to my grandparents, who have always shown great excitement in my studies. And, to my dear parents for their eternal support and love. Thank you all for making my many years of study possible. Last but not least, a big thanks to my fellow students and friends who are always up for a scientific discussion and making my two years at the University of Oslo the most memorable and fun years of my life.

Petter André Kristiansen
July 2019
Oslo, Blindern

Chapter 1

Introduction

In top-level sports, the equipment plays a significant role in the performance of athletes. Technology is becoming a leading factor in finding the right features in the equipment to increase the performance of athletes. This can be seen especially in cross-country skiing. Athletes take pride in saying they have the best ski equipment. The best results in competitive cross-country skiing are achieved when the athlete is performing at his or her best level. However, this is only possible when the athlete is using skis with the mechanical properties suiting the athlete and the current snow conditions.

A large field of research already exists around mechanical properties in cross-country skis. A deeper understanding of these mechanical properties is not readily available to many. Often, these mechanical properties are kept secret by the manufacturers to keep a cutting edge in performance over rival manufacturers. Finding the skis with the best mechanical properties is of utmost importance. As an example, Bäckström, Dahlen, and Tinnsten (2008) published a paper describing a ski measurement system the Swedish cross-country team in 2008 had been using for 2.5 years to match mechanical properties in skis. This resulted in faster and more accurate matching of cross-country skis.

Making a selection of skis with matching mechanical properties for an athlete is essential for performance. The problem is finding the right mechanical properties for different weather conditions. This thesis investigates one such mechanical property of classical cross-country skis: the pressure distribution. The pressure distribution can be a defining factor in choosing proper skis for an athlete.

1.1 Objective of thesis

The main objective of this thesis was to create a measurement setup using cheaper commercially available pressure-sensitive film sensors to investigate the mechanical property pressure distribution in skis. It was desired to investigate if the results gave reliable indicators on the difference between cross-country skis for warm and cold weather and snow conditions. The second objective was to investigate if the pressure distribution could give indications of twisting in the cross-country skis. These indications could be seen by comparing the forces on either side of the skis. The third objective was to investigate the pressure distribution characteristics when offsetting the position on the skis where the force is applied. To measure the forces being transferred from the cross-country ski to the surface, a mechanical system was developed. The mechanical system was developed with commercial force sensors placed along a measurement block placed in the system. The measurement system proved to give somewhat consistent results with deviations in the output for a selection of the sensors. The process of designing a mechanical system is described in three chapters. Chapter 3 focuses on developing the mechanical design of the measurement system, while Chapters 4 and 5 focus on developing the required electronics to conduct measurements. Due to the faulty design of the simulated foot for offset measurements, the third objective was discarded. The pressure distribution of cross-country skis was instead only investigated for loads directly on the binding point of the cross-country skis.

This thesis consists of three major parts of *Materials and Methods*, that make out the process of creating a measurement setup. Due to the broad scope of subjects, the thesis is divided into three main components with individual results and discussions. These three components are then brought together to produce the main results and discussion. This structure is based on a modified version of the *IMRaD* model from Day (2011), which allowed for summarizing and discussing important factors in each part before continuing to a new subject. This was done to allow for partial conclusions to be drawn, which helped to make decisions in the following parts of the design process.

The thesis seeks to answer the following research questions:

A How can the pressure distribution of skis be measured using commercially available force sensors?

B How can we identify twisting in cross-country skis?

1.2 Key results

The mechanical property pressure distribution can be used to investigate the different weather and snow conditions suited for each ski measured. The pressure distribution gives solid indicators of pressure zones and how they relate to weather and snow conditions. It was found that the mechanical system in this thesis operates with more significant deviations in the measurements due to the inaccurate calibration of the sensors. Therefore the system cannot produce reliable results in its current state. The time-drift factor for each of the sensors had a significant impact on the calibrations and measurements, thus considering this factor with new calibrations, the mechanical system can be used to collect pressure distribution data from cross-country skis quantitatively. With further tuning of the sensors, circuits, and calibrations of the system, more reliable results with higher accuracy and precision can be produced. Even though the accuracy and precision of the system were poor, a clear difference in each ski measured was seen. Twisting of cross-country skis could not be confirmed due to the current accuracy and precision of the system.

1.3 Thesis outline

Chapter 2 explains the concept of cross-country skiing and considers the important mechanical properties in cross-country skis. These mechanical properties are key features that contribute to the skiers overall performance.
Chapter 3 focuses on the mechanical design of the measurement system. A process going from initial concept phase to finished product is presented throughout the chapter. We discuss important abilities of a measurement system and manufacture a mechanical system in aluminum to conduct measurements of cross-country skis.
Chapter 4 investigates the sensors required to register load transferred from a cross-country ski to the surface. We investigate important features and characteristics of how the sensor behaves under load like time-drift and variations in the sensor.

Chapter 5 explains which circuits that are required to sense the changes in the sensors. Different circuits are evaluated to produce circuits with low noise output and low power consumption.
Chapter 6 pulls Chapters 3 to 5 together to produce digital measurements. This chapter explains what is used to represent the load from the sensors digitally. Calibrations and software are explained and give indications of measurement quality from the sensors.
Chapter 7 presents the main results from the digital measurements. The chapter includes pressure distributions from the ski measurements and calculates the measurement quality. Heat maps are produced to visualize the pressure distribution.
Chapter 8 discusses the results presented in Chapter 7. We investigate the difference in the measurements and draw assumptions on the difference between cross-country skis for warm and cold weather conditions.
Chapter 9 concludes this thesis. We draw conclusions on what the measurement system is able to do and what can be interpreted from the measurements. We then discuss potential improvements to the system for future work.

Chapter 2

Background and theory

Chapter abstract: *In the mid-twentieth century, various measurement devices were developed to investigate the mechanical properties of structures such as skis. The importance of conducting objective testing and selection of cross-country skis for competitive skiing is important. It is often claimed that roughly* 80% *of the total performance of a cross-country ski is based out of mechanical properties of the skis, such as span curves, camber height, and pressure distribution whereas the skier and service personnel influence the remaining* 20% *through grinding and waxing (Rønbeck and Vikander 2007; Rønbeck 2001). This chapter does a brief review of the existing ski measurement systems, presents the mechanical properties of a ski, and a brief description of the physics behind why a ski glide.*

2.1 Cross-country skiing

Cross-country skiing is a whole-body endurance sport where the skier uses a combination of poles and skis to generate speed across snowy terrain. This sport is used by many as a family and recreational activity, but also for a competitive purpose. The goal in competitive skiing is to reach the finish line in the shortest amount of time. In modern competitions, the winning margins are minimal. During a World Cup race on March 2018, the time difference between a first and fourth place was from 1.1% for men to 2.3% for women on the overall standings (FIS cross-country 2018). In other words, the difference between a losing and winning pair of skis in competitive skiing is minimal. The need for precise and reliable selection of professional skis increase, since selecting the best pair of skis is crucial. The importance of ski properties has been studied in multiple scientific publications, such as in Rønbeck and Vikander (2007). Cross-country skiing consists of two different

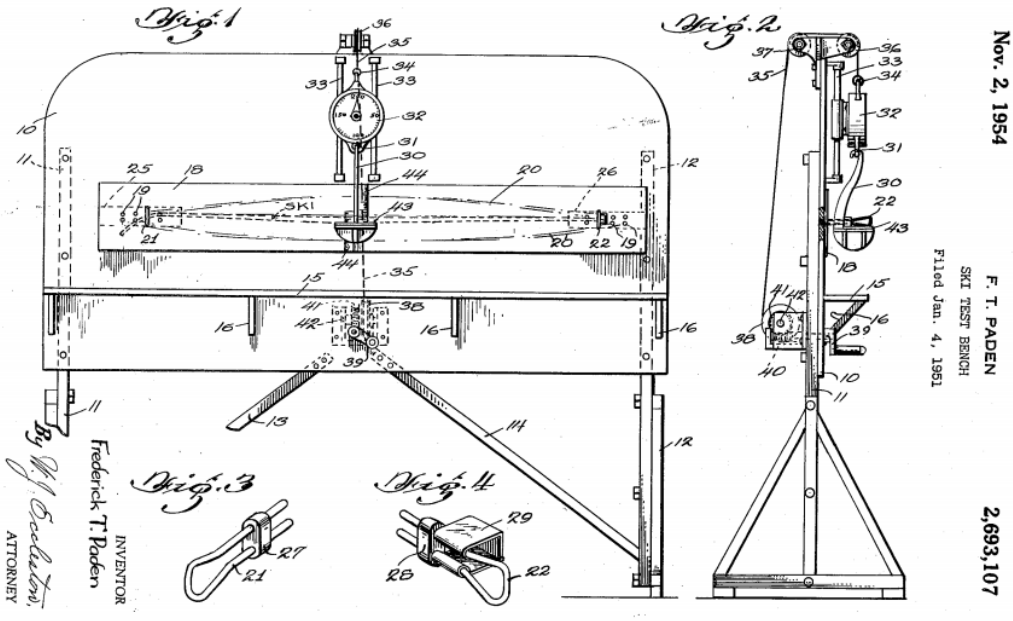

Figure 2.1: Illustrating the concept of a test bench. Figure from Paden (1954).

techniques; the classical style, and the skating style. Different type of skis is used for the two different styles since classical skiing requires skis that can help both grip and glide while skating style skis only need to glide. In this thesis, however, we restrict ourselves to the ski's used for classical style skiing.

The performance of a cross-country skier is highly dependent on the performance and quality of the skis. The ski's performance is determined by several mechanical properties such as the camber height, stiffness and pressure distribution (Bäckström, Dahlen, and Tinnsten 2008; Erkkilä 1986). These characteristics will be explained in detail in Section 2.2. Another vital factor for the performance of the ski is the wax applied under the skis, both the grip wax to make the ski grip and the gliding wax to make the ski glide (Breitschädel 2014). However, it is often claimed that the performance of the skis themselves are roughly 80% of the total performance, while the remaining approximately 20% is influenced by the skier and service personnel (Rønbeck and Vikander 2007; Rønbeck 2001). Grinding of the ski sole represents roughly 10% and the waxing also only 10%.

Finding the best pair of skis is a challenge. Skis are chosen by the athletes and the experts together to find the best fit for the athlete. Great resources and time are being spent on manually selecting a large pool of skis for testing

in the field (Breitschädel 2014). The skis are hand-picked with tools from the manufacturers by experts with intuition and experience (Bäckström, Dahlen, and Tinnsten 2008). The only quantitative measurement available to the experts is the span curve (introduced in Section 2.2.1), and thus the selection is much based on the expert's subjective non-quantitative judgment of a ski.

The skis from the stored pool are then used for further testing. The manual selection can indicate that the differences in each ski selected are prone to human error in terms of subjective selection. Furthermore, a quantitative way of choosing skis can further improve the ski selection phase by performing objective measurements and selection of cross-country skis.

Older methods of testing mechanical properties in materials were done by applying force to the middle of a structure. A measurement device, like the one shown in Figure 2.1 was typically used to investigate the elasticity of structures like aircraft wings or skis. The concept was to apply forces to the center of the structure to determine deflection or stress. Companies like *SkiSelector* (see Section 2.4.2) and *Eiker Måler* (see Section 2.4.1) have developed measurement devices with similar concepts, with focus on measuring the height of the camber and stiffness when applying an external force on the ski. By measuring and collecting mechanical properties, these measurement systems can give each ski a span curve profile used for matching similar skis, and finding skis suitable for different athletes and conditions.

2.1.1 Body weights and loading Weights

When collecting mechanical properties during measurements of skis, it is necessary to load the ski with the correct weight, based on the weight of the skier, for the matching the two different ski-phases. These ski phases are the kick phase and the glide phase. The full body weight (FBW) of the skier is loaded to find grip zones. The stiffness of the ski determines the amount of contact with the grip zone during kick-phase for different weather conditions. These weather conditions are warm, zero, and cold weather. During the gliding phase, the skier balances the weight equally onto both skis to avoid the gripping wax from getting contact with the snow surface. For this phase, the weight loaded on the ski is defined to be the skiers half body weight (HBW). These weights represent the loads applied on the ski for collecting the mechanical properties of the ski, during kick phase and gliding phase. The binding point (BP) is defined for this thesis as the point on the ski where the shoe tip attaches to the ski binding. It is the reference point of where to apply forces, either at the binding point directly, offset towards or away from the heel point. When investigating the skis quality and ability to glide, it is necessary to analyze the mechanical properties of the ski at the

skiers half body weight.

2.2 Mechanical properties

A cross country ski has many mechanical properties. The mechanical properties are also referred to as characteristics. These are essential when describing and measuring the quality of a ski. The mechanical properties can be; arch, stiffness, and pressure distribution, which describes how the weight distributes along the longitudinal length of the ski. Choosing skis with mechanical properties matching the weather conditions is an essential way of finding the right skis. Several scientific publications exist, but, e.g., Breitschädel (2014) published several papers on different aspects of how the gliding speeds and overall performance can be improved by using skis with different mechanical properties and sole structures.

2.2.1 Span curve

The span curve is the curvature of a ski profile that represents the camber height along the longitudinal length of the ski at HBW or FBW (Rønbeck 2001). As shown in Figure 2.2, the force is applied at the balance point. The span curve is extracted by pushing the ski down with the skier's FBW, followed by measuring the height from the surface to the ski sole. The span curve is further used to determine the flex and stiffness of the ski and is essential for finding suitable skis for different weather conditions.

2.2.2 Camber height

The mechanical property camber height is described as the height from a flat surface to the sole of the ski and can be found from the span curve. The purpose of looking at the camber height at FBW and HBW is to find the contact area for gripping wax to be applied; this area is also referred to as the camber pocket. Typically, the skis are marked on the side of the ski to indicate different chamber heights. One of the camber heights is often marked at $0.2mm$. Preferably, this height is when FBW is loaded. Contact is defined as the camber height at $0.05mm$ (Breitschädel 2014). Marking the waxing zone at FBW results in the gripping wax not establishing contact with the snow during the gliding phase. The purpose of the marks is to define the gripping area on the sole, so the gripping wax establishes contact with the surface during the kick phase (Breitschädel 2012). Furthermore, the definition of camber response is the change of camber height per Newton

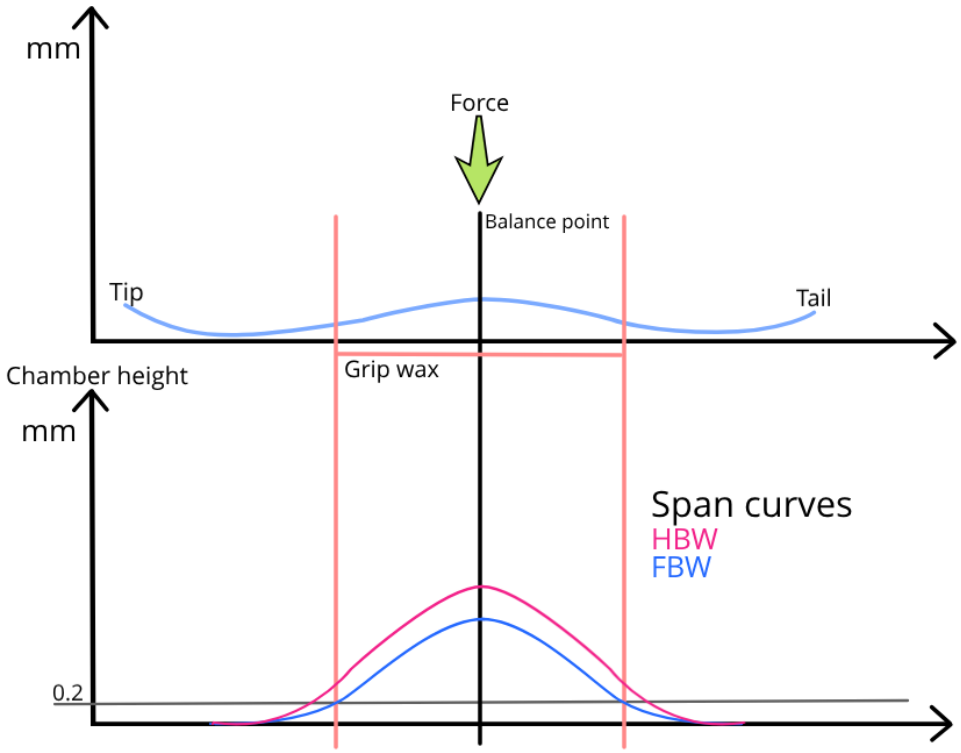

Figure 2.2: An illustration of the span curves with HBW and FBW.

(mm/N). The camber response is found by loading the BP from 0.5 to 1 times the body weight. The camber response is used to calculate the stiffness of the ski (Breitschädel 2014).

2.2.3 Stiffness

Stiffness is the skis ability to withhold forces. It is when selecting a matching pair of skis, for stiffness at FBW and HBW. Stiffness contributes to giving the wanted camber heights and span curve profiles for individual users concerning their body weight. The stiffness is essential when finding a pair of matching skis for the different weather conditions. The stiffness, k, is the relation between the skier's body weight and the camber response of the ski (Breitschädel 2012).

2.2.4 Pressure distribution

Pressure distribution is a mechanical property that describes the transferred forces to the surface along the longitudinal length of the cross-country ski

(Bäckström, Dahlen, and Tinnsten 2008). Pressure distribution characteristics are obtained by measuring the forces on the surface were the ski presses down. The purpose of measuring the forces at specific points is to find hot spots of forces on the surface which contributes to frictional melting (see Section 2.3.1), and how the ski structure distributes weight along the surface from the ski. Further on, fluctuation in the ski structure under stress indicates the ski quality in terms of twisting and even weight transfer along the latitudinal length of the ski. The pressure distribution can work as an additional property for finding a suited match of skis for an athlete. Nilsson, Karlöf, and Jakobsen (2013) researched how the force distribution changed when the loading point (center of mass) moved backward from the original BP position.

Figure 2.3: Ski test bench developed by Felix Breitschädel. Figure from Breitschädel (2014).

2.3 What makes a ski glide?

A ski is gliding when the positive forces generated by the skier is larger than the negative forces working on a skier (Section 2.3.2). Positive gravity forces are generated either from going downhill or during kick-phase, resulting in gliding speeds. Overcoming the negative forces are essential for the performance of the skier. A ski slipping or gliding on the snow surface is dependant on the amount of friction between the ski sole and the surface. The friction and speed determine the amount of frictional melting (see Section 2.3.1) that occurs on the ski sole. The frictional melting of snow or ice generates a thin layer of water film, which decreases the friction. Snow and ice structures determine the amount of water film and friction that is needed. Different characteristics of the snow and snow crystals are not the aim of this study. Detailed characteristics on snow types and snow crystals were researched by

Colbeck (1986) and are to the author's knowledge the most recognized and used classification scale for snow. Nevertheless, an understanding of how the forces are affecting the skier's total performance is necessary to investigate.

2.3.1 Snow and ice friction

Friction between a ski sole and snow or ice surface is highly dependant on; weather, temperature and snow conditions (Rønbeck 2001). Factors like the ski characteristics contribute to overcoming the negative forces and the delicate balance between friction and water film. A water film is a thin layer of water gathered up on the ski sole during skiing. It is determined by the friction coefficient μ between the ski sole and the surface. This layer is a result of snow or ice melting due to frictional melting and works as lubrication for improved gliding speeds. The change in the friction coefficient as a result of frictional melting was already researched in the mid-nineteenth century by Bowden and Hughes (1939). They found that the friction coefficient decreased when the water film is introduced to the polyethylene sole surface (Bowden and Hughes 1939). Furthermore, a conclusion was derived that the friction was also related to temperature. Bowden and Hughes (1939) found that a decrease in temperature would increase the static friction, indicating lower friction in higher temperatures. When sliding speeds are noticeable, the friction decreases and approach a lower value, increasing speeds further decreases friction due to a localized surface melting produced by frictional melting (Bowden 1953). A thicker water film is not always the best case for any weather condition. When the water film accumulated exceeds a threshold, the water film generates drag, which results in reduced gliding speeds. More detailed research on the relation between the contact area with the surface and the water film thickness was conducted by Bäurle et al. 2006. The increased contact area with the surface with growing water film thickness is illustrated in Figure 2.4. As friction is affected by the gravitational forces as well as the accumulated negative forces on the cross-country skier, it is in our best interest to investigate these for understanding which skis characteristics that contributes to better gliding speeds.

2.3.2 Forces working on the skier

In cross-country skiing, propulsive forces are generated through the skier's activity using a combination of poles and kicking. The objective in cross-country skiing is to generate speeds by overcoming the negative forces, such as air resistance, drag, and friction. The forces acting on a skier in a gliding

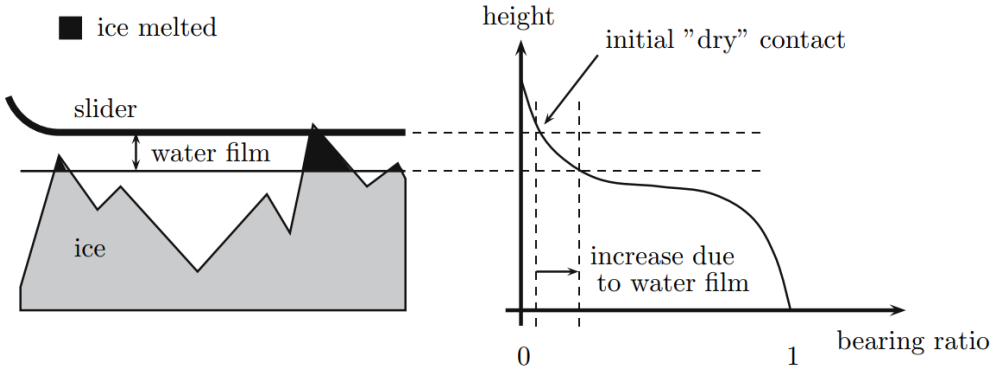

Figure 2.4: Relation between the water-film thickness and the real contact area (bearing ratio). Melting of ice corresponds to a slicing off and leads to the growth of existing contact and the formation of new contacts. Figure from (Bäurle et al. 2006).

scenario is illustrated in Figure 2.5. We will follow the central derivations and findings from Breitschädel (2014):

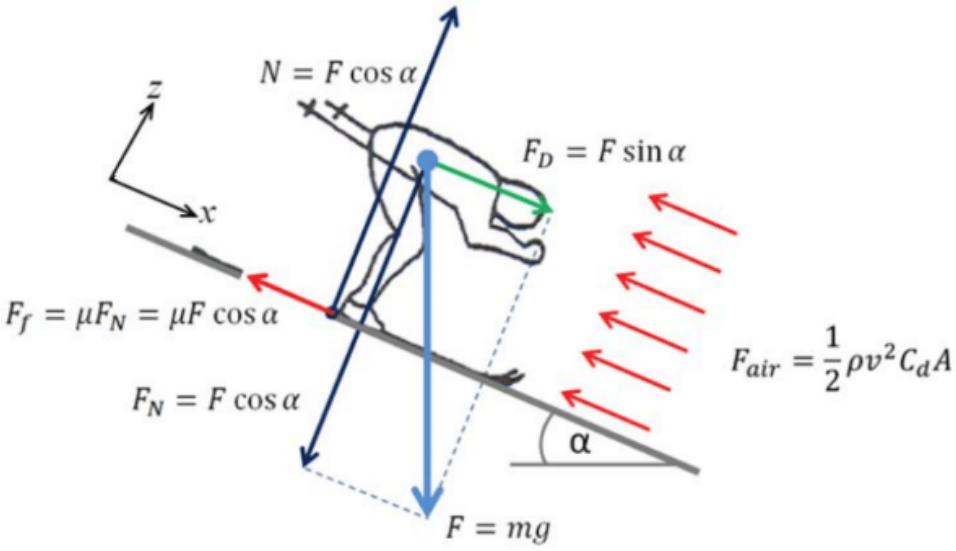

Figure 2.5: The forces acting on a skier. Figure from Breitschädel (2014).

According to Newton's 2nd Law, the forces in the direction of motion x are equal to the skier's mass m times the acceleration a:

$$\sum F_x = ma. \tag{2.1}$$

The skier's propulsion is affected by force F_D while gliding, which is the mass m times the gravity g on an inclined surface:

$$F_D = F \sin \alpha = mg \sin \alpha \tag{2.2}$$

The negative forces working against a skier's propulsive forces are air resistance F_{air} and, the frictional forces working between the snow or ice surface and the ski sole F_f. The total sum of forces from Equation 2.1 become:

$$F_D - F_{air} - F_f = ma. \tag{2.3}$$

The friction coefficient μ is defined as the resistance force F_f divided by the downward working force F_N:

$$\mu = \frac{F_f}{F_N} \tag{2.4}$$

The static friction coefficient μ_s is found when the ski is just about to slip, i.e., $F_D = F_f$:

$$F_D = F_f, \tag{2.5}$$

i.e.,

$$mg \sin \alpha = \mu_s mg \cos \alpha. \tag{2.6}$$

We can rewrite Equation 2.6 with regard to μ_s:

$$\mu_s = \tan \alpha. \tag{2.7}$$

On the other hand, the kinetic friction coefficient μ_k is of interest when the ski is gliding:

$$F_D - F_f = ma. \tag{2.8}$$

Writing out the equation for kinetic friction, we get:

$$mg \sin \alpha - \mu_k mg \cos \alpha = ma,$$

i.e.,

$$\mu_k = \frac{g \sin \alpha}{g \cos \alpha} - \frac{a}{g \cos \alpha}.$$

The equation can be used for both kinetic and static frictional forces. The intervals can be defined as the following:

$$\mu_k = \begin{cases} \mu_s & \text{if } a = 0 \\ \mu_s - \frac{a}{g \cos \alpha} & \text{if } a \neq 0 \end{cases} \tag{2.9}$$

The adjusting factor when applying the right gliding wax for warm-, zero- or cold-weather conditions, is the amount of kinetic friction between the snow or ice surface and the ski sole. Equation 2.9 denotes that the kinetic friction coefficient is equal to the static friction coefficient when the acceleration is zero. At zero acceleration, the skier is in a gliding phase or standing still. The gliding wax can either reduce or increase the kinetic friction coefficient to give enough water film for better gliding speeds.

2.4 Measurement devices

The span curve is an essential descriptor of the mechanical properties of the ski. Several measurement devices have been developed to efficiently and accurately measure the span curve and camber height. The following sections present previous research on measurement devices and existing methods for extracting mechanical properties.

2.4.1 Eiker måler

The Eiker ski measurement device was initially developed for the winter Olympics in Lillehammer in 1994 by a Norwegian company called Ski-Test (Ski-Test 2018). The idea behind the Eiker-måler was to pair skis with similar span curves and to find a reasonable match to the skier concerning stiffness to weight ratio. Since the start of Ski-test, they have been developing their system with great success. It has expanded to several countries, such as Sweden, Estland, Canada, and the USA, to mention a few (Ski-Test 2018). As instructed by the company Ski-Test (2018), the electrical measurement device loads the ski with a skiers weight to HBW and FBW to mark the gliding zones and kicking zones for application of gliding wax and gripping wax respectively. The Eiker-måler can be seen in Figure 2.6.

2.4.2 SkiSelector

SkiSelector is a Swedish company, with the first SkiSelector system developed for the winter Olympics in Turin in 2006 (SkiSelector 2018). It has increased in popularity since 2006, and in 2011 the SkiSelector Academy was founded to develop the system further. The system delivers a good overview of skis mechanical properties such as grip, stiffness, camber characteristics, and sliding properties. The goal of this system is to give the skier detailed information about the pair of skis and how the skis should be waxed for

Figure 2.6: An illustration of the "Eiker-måler". Figure from Ski-Test (2018).

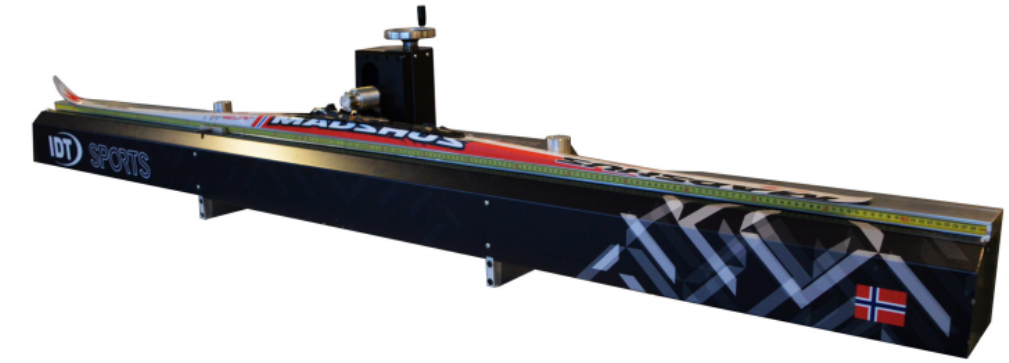

Figure 2.7: An illustration of the SkiAnalyzer from IDT Sport. Figure from IDT Sport (2018).

better grip and glide (SkiSelector 2018). The system looks similar to the "Eiker-måler". In addition, the SkiSelector uses a computer with software to create and store ski profiles of each ski measured.

2.4.3 IDT Sport - SkiAnalyzer

The SkiAnalyzer from IDT Sport delivers a complete measurement system with different software versions matching the user's experience (IDT Sport 2018). The measurements are based on laser technology to measure the camber height and stiffness. Through the software, the system outputs span and stiffness curves. Furthermore, at the end of a measurement, the user can save the measurement data to a database for later use (IDT Sport 2018). The information provided by IDT Sport is limited. The SkiAnalyzer system seen in Figure 2.7 seem to operate with the same precision as SkiSelector and Eiker Måler.

Figure 2.8: Figure show a ski placed ontop of the Gear West Signature Flex tester, image taken from Gear West (2011).

2.4.4 Gear West Signature Flex Tester

Gear West developed the system Ski DNA (Gear West 2018). The system consists of three phases for choosing and measuring cross-country skis, where the first phase is using hands and eyes when squeezing the skis. After the subjective selection, the skier will apply body weight in different positions on the ski. By loading the ski, the gripping zone of the ski is found to ensure that the selected skis match each other. The third phase is to put the skis through the Flex Tester measurement bench. The measurement bench, shown in Figure 2.8, is designed to use loading cells to collect pressure distribution data. This data allows the system to check the quality of the flex, weight range, and ideal snow condition for the skis.

2.5 Chapter discussion and conclusion

Mechanical properties will always be a defining factor between a winning and losing pair of skis. Selecting the right ski for different weather conditions has a significant role in the ski selection phase. A stiffer ski with a short nominal running surface is typically found in classical cross-country skis for warm-

weather conditions, giving a steeper increase in camber height at the start of the wax pocket. Warm-weather conditions require a stickier grip wax which introduces a thicker layer of wax. The steep increase in camber height decreases the probability of the gripping wax in the wax pocket and reducing the chance of getting contact with the surface during a gliding phase. On the contrary, a ski with a more extended nominal running surface is found on classical cross-country skis for cold weather condition. The gripping wax has a dryer consistency, which reduces the overall height of gripping wax applied. The extended nominal contact area will also introduce more frictional melting for generating more water film for better gliding speeds in colder weather conditions.

Based on how the athlete's body weight is loaded on the ski, by for example different pressure points of the foot, varying results in pressure zones onto the ice or snow surface occurs. The thought is that a stiffer structure on the inside of a ski can be countered by a matching weight profile of the foot with extended pressure on the inner side of the foot, resulting in an overall flatter contact of the latitudinal running surface of a ski. With this in mind, it is possible that the friction is more evenly distributed on the surface, resulting in more consistent heat generation and water film due to frictional melting of ice or snow.

The Ski DNA system (Section 2.4.4), is by far the most interesting. More specifically, the use of loading cells to measure pressure distribution. By using loading cells on prefixed location along with the longitudinal running surface of the ski, we can investigate the forces on each of these points. This investigation could result in pressure distribution profiles for assisting in ski selection. Breitschädel explained that a measurement uncertainty with the Ski Analyzer (Section 2.4.3), was affected by the ski running surface. Some sensors on the system could not register contact with the ski, due to the twisting in the skis material. To the author's knowledge, twisting in the ski structures is a result of deformation of the materials in the ski under production. Finding skis with minimal twisting can result in a more evenly distribution of weight onto ice or snow surface. The lack of knowledge on twisting and pressure distribution profiles on classical cross-country skis motivates the development of a measurement device to register both. In this thesis, a measurement device is researched and designed to investigate mechanical properties in classical cross-country skis, specifically the pressure distribution. In the following chapters, the prototyping of a measurement device for evaluating the pressure distribution of cross country skis is developed. The prototype builds on existing research and designs inspired by multiple sources, such as Rønbeck (2001) and Breitschädel (2012, 2014).

Chapter 3

The mechanical design

Chapter abstract: *Concept to finished design of a mechanical system is explained in detail in this chapter. The first part of the chapter goes through the first ideas and concepts from drawings to the first 3D-model of the mechanical design. The concept of the mechanical design is further developed with the intention of being operated by a single person. The second part elaborates on how the mechanical design evolved from a simple design to more complex 3D-models of the overall design with ideas of implementing a linear weight guide to handle the loading of weights. The third part of the chapter digs deeper into improving the mechanical design. Details around the design of pocket holes for sensor placement and a tool for calibration is explained. Key features like handles on the linear weight guide for operating the mechanical system, weight transfer pins and locking mechanisms for a ski binding is considered and as a result, contributes to the improvement of the design. The final part of the chapter consists of final representations and testing of the mechanical system.*

3.1 Initial phase

The initial concept phase of designing and manufacturing a mechanical system focused on deciding and establishing what properties the system should possess. Our goal was first and foremost to collect pressure data along the longitudinal and latitudinal lengths of a cross-country ski. From the discussion regarding the importance of the pressure distribution of the ski from Chapter 2, we would like to develop a mechanical system that could place sensors at multiple points underneath the ski. An initial prototype of such a mechanical design is shown in Figure 3.1. The prototype was developed in an earlier student research project by Ole Marius Rindal and Jacob Norenberg

(Rindal 2017, *personal communication*, December), and can be considered the initial concept of the mechanical design of the prototype developed in this thesis. The objectives of the first concept were;

1. Collecting the measurements of the pressure on multiple points along the ski.
2. Repeatable measurements with low variance.
3. Detect differences in a wide range of skis.
4. Detecting deflection and twisting in the structure of ski under load.

However, this first prototype had some shortcomings, as for example, the lack of *pucks* to precisely place the load of the force on the sensors leading to unreliable measurements.

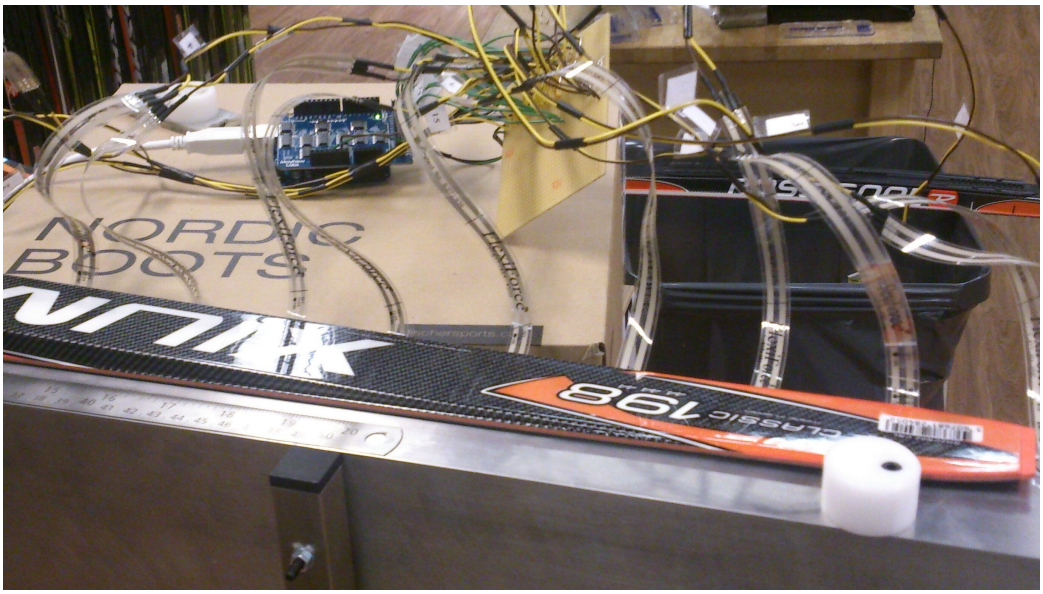

Figure 3.1: Photo of student research project led by Ole Marius Rindal and Jacob Norenberg (Rindal 2017, *personal communication*, December).

3.2 Concept one

The first sketch of an improved mechanical design consisted of a polymethyl methacrylate plate (plexiglass) as a top and bottom surface, enveloping the sensors. The top plate of the measurement block illustrated in Figure 3.2

had holes drilled out directly above the sensors, working as a guide for a piston to transfer weight from the ski to the sensor. Enveloping the sensors between two plates, would result in accurate placement of the sensors and locking it in position to avoid movement of the sensor.

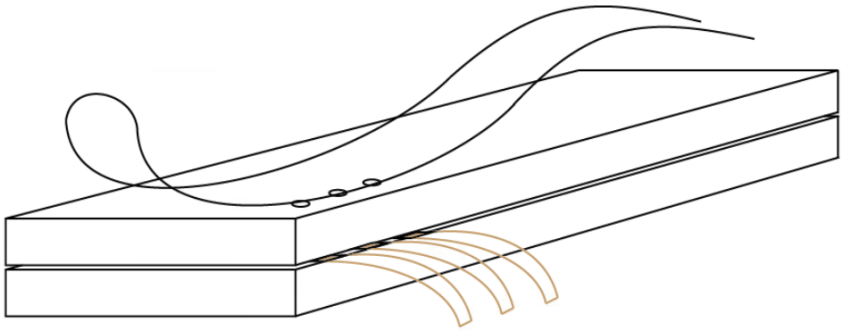

Figure 3.2: Early concept on sensor placement and structure, computer drawn.

3.3 Concept two

To be able to apply the force representing the full body weight (FBW) and half body weight (HBW) vertically down on cross-country skis, and to calibrate the sensors, one would need a digital weight press or manual weights applied on the ski. During the investigation of possible ways of applying this weight to the system, there were no accessible alternatives. After consulting with the Instrument Laboratory (I-Lab) at University of Oslo, Department of Physics, we concluded that the bottom surface had to be more rigid than plastic and would need to withstand bending when applying force. The polymethyl methacrylate plates from concept one were not suited for this task, changing the choice of material to aluminum. I-Lab proposed a solution for applying weight on the ski linearly with a linear weight guide shown in Figure 3.3.

The linear guide on its own would not be placing the weight accurately on the ski. A 3D-modelled version of the sketch was drawn with the idea of using aluminum for the whole frame, giving the bench more stability and making it stiffer. The 3D-modelled sketch seen in Figure 3.4 and 3.5 was drawn in AutoDesk Fusion 360 to visualize the concept of the mechanical design. It became clear that the sensors would need pockets to be placed in the bottom plate to avoid squishing between the plates. The squishing

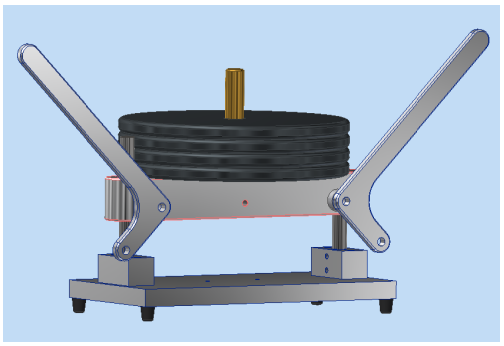

Figure 3.3: Concept for applying forces linearly on a surface.

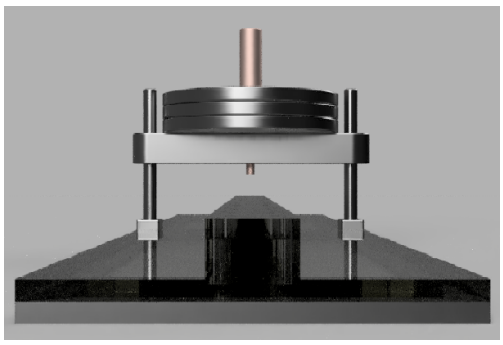

Figure 3.4: 3D-model of concept two, Front side.

would lead to errors in the measurements due to external forces from the plates onto the sensor.

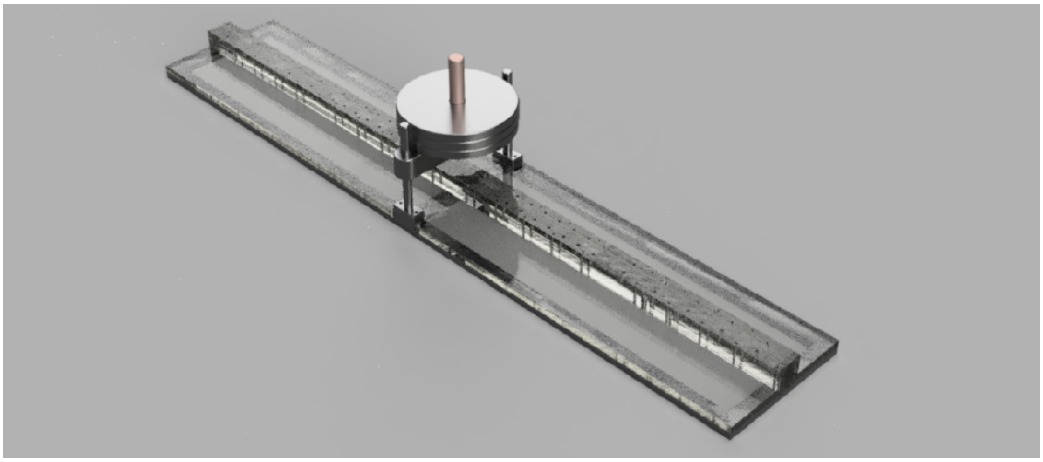

Figure 3.5: 3D-model of concept two.

To produce a mechanical system of this size and precision, we needed a specialized computer numerical control (CNC) machine for accurate placement of the sensor pockets and alignment of assembly points for bolts. Further consultation with I-Lab resulted in assisting this master project by producing the mechanical frame with the needed precision, based on the 3D-model from Figure 3.5. The most significant changes in concept two, compared to concept one, were the combination of an aluminum frame with a measurement surface and the linear weight guide attached. These three components together came to be the final result of concept two. With this in mind, additional development was necessary, in terms of functionality, sensor placement, and locking of the binding to hold the cross-country ski.

3.4 Concept three

The final concept required more functionality of the mechanical system. These functionalities were eased operation difficulty of the bench, ergonomics, and the possibility of calibrating of the sensors. One of the more significant changes from concept two to concept three were the changes done to the measurement block containing the sensors. Small pockets were introduced for the sensors to be placed accurately. The design of the pockets focused on a perfect fit of the circumference of the sensor explained in Section 4.2. The choice of sensor is explained in detail in Chapter 4. As Figure 3.6 shows, the pocket holes guiding the sensor with an underlying puck (or piston) for a pinching effect on the sensor. This pinching effect was described to give more accurate results in measurements, using pucks on either side of the sensor (Vecchi et al. 2000). The pucks needed to cover at least 80 % of the measurement surface on the sensor for optimal accuracy (Fraden 2005, 10.3, p.418). Pockets on the measurement block were placed with a center-to-center distance of 25 mm along the longitudinal length with a total length of 215 cm. A second row with a center-to-center latitudinal distance 30 mm was added for the ability to extract sensor values in a two-dimensional manner. The number of pocket holes created increases the flexibility of moving sensors, thus leaving an excessive amount of pocket holes. The sensor placements could then be adjusted to areas of interest for individual cross-country skis. The linear weight guide was placed in the middle of the frame to load the weight linearly down on the binding point of the ski. An additional plate representing a foot was attached to the linear guide with the option of adjusting the position of load offset from the binding point. The thought of the adjustable plate was to investigate pressure distribution characteristics at different resting positions during the gliding phase. A locking mechanism was placed on the bottom of the linear weight guide to lock the cross-country ski in position at the binding of the ski.

The upper part of the measurement block had holes of 10 mm drilled out, for brass pistons or weight transfer pins (WTP) to be placed. As described earlier in this section, this would create a pinching effect on the sensor with the pockets (Vecchi et al. 2000). These upper pistons of 9.8 mm were designed with a detachable plastic cap with threading. These rounded plastic caps were used for free movement of the ski on top of the WTP.

The side handle on the linear weight guide, which can be seen in Figure 3.3, was introduced to increase ergonomic use and lower the difficulty of handling the system. The handles are placed to reduce the amount of force needed to pull the guide up for replacement of sensors and changing skis.

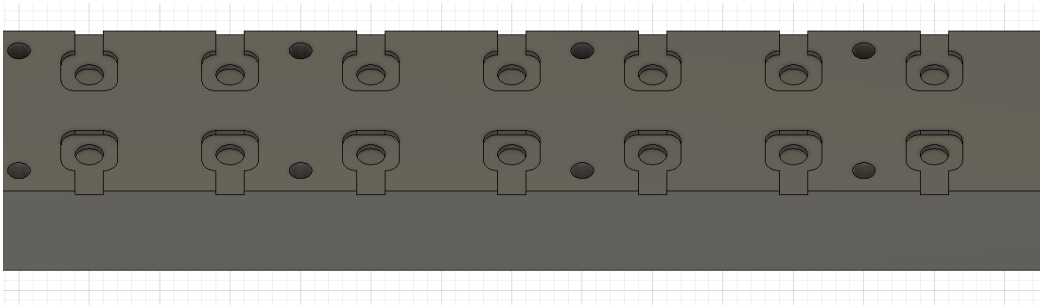

Figure 3.6: 3D-model of the pockets for sensor placement.

An additional tool was designed for calibration of the sensors. An aluminum beam attached on the center between two supporting legs which would rest on the frame of the mechanical system is shown in Figures 3.7 and 3.8. At the end of the beam, a switchable loading point was attached to load individual sensors at the beam location. Weights would then be placed on top of the center of the beam, transferring the half of the loaded weight on to the sensor. When a calibration of the sensor was conducted, the measured values would represent the pressure. Details on calibrations is explained in Section 6.3.

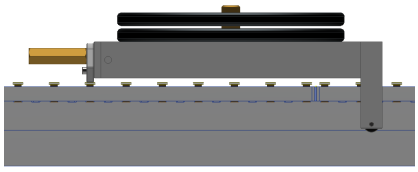

Figure 3.7: 3D-model of the calibration tool, side view.

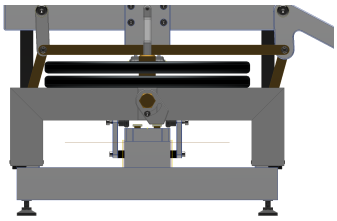

Figure 3.8: 3D-model of the calibration tool, front view.

3.5 Chapter results

The last and final concept of the mechanical system was assembled and is illustrated in Figures 3.9 and 3.10. The final concept with all parts assembled to complete the mechanical system is shown in Figure 3.11.

The mechanical frame with the linear weight guide was manufactured and assembled by I-Lab specifically for this master project. After the construction and assembly, the frame was transported to the Department of Informatics for

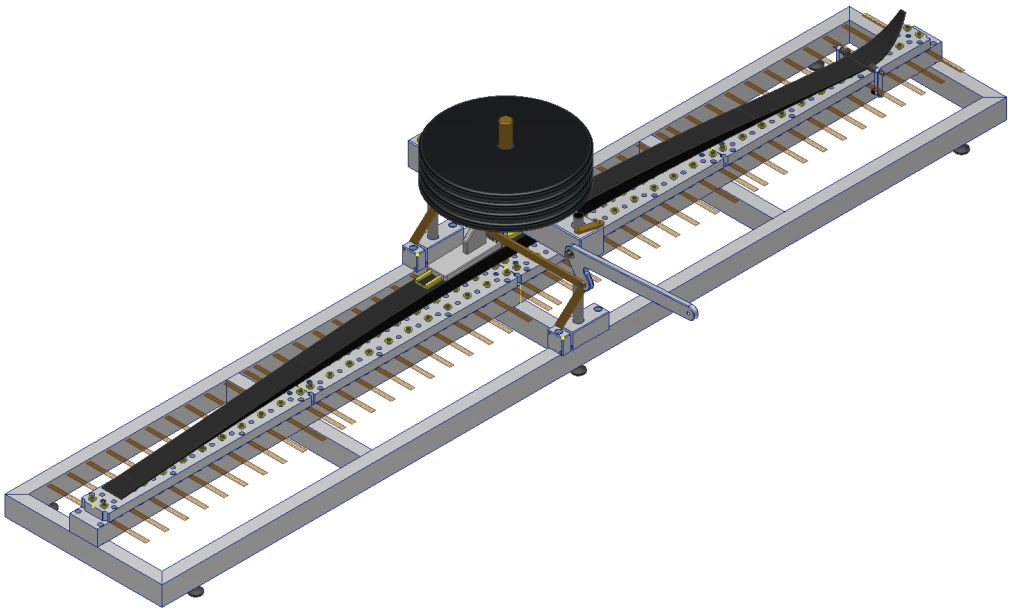

Figure 3.9: 3D-model, final concept, home view.

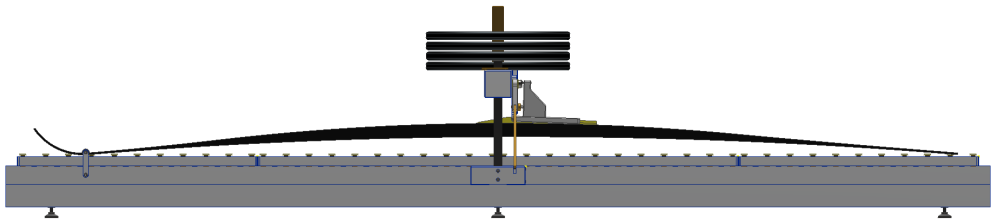

Figure 3.10: 3D-model, final concept, side view.

installation of sensors and circuits. The mechanical frame weighted around 40 kg and had 6 feet with adjustable height to level the system. The initial

tests of the mechanical system showed that the adjustable foot was designed for a different binding and could not be used; instead, we were only able to apply pressure on the binding point. The loading point of the calibration tool designed was not centered on halving of the loaded weight on to the pressure point. A digital kitchen weight with $\pm 1g$ accuracy was used to measure the difference between the total weight of the calibration tool and the weight at the pressure point (Rubicson 2019). The ratio was found to be 0.5072, which was used to multiply the loaded weight for accurate weights on the pressure point during calibration.

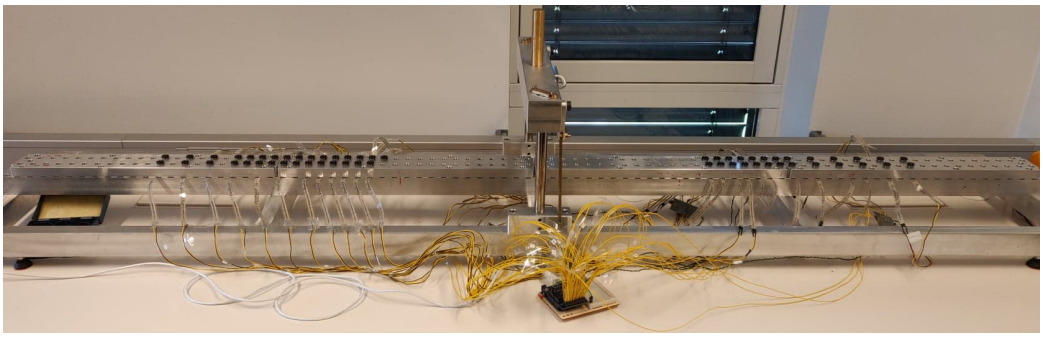

Figure 3.11: Finished assembly of mechanical system, with sensors, circuits and microcontroller.

3.6 Chapter discussion and conclusion

The initial idea of investigating how the pressure distribution from a single ski differs with the force applied to an offset from the binding point was not possible due to the faulty design of the adjustable foot. The time needed to redesign the adjustable foot was not a priority due to the time limit of this thesis. The foot could produce interesting results when loading the weight at different offsets from the binding point. The offset would, in theory, represent the pressure loaded closer to the heel of a cross-country skier in, for example, the tucking position when gliding. However, as with most modern ski bindings, the binding can be moved to different offset positions compared to the balance point of the ski resulting in similar effects. Upon delivery, the mechanical system showed great promise to handle the required properties. Initial testing of the linear weight guide was done using 45 kg. The lifting and lowering of the weights could easily be done using the handles, thus making the system easy to operate. A cross-country ski was attached to the loading point of the linear weight guide for an initial test run. The test showed that

the weight transfer from the weight guide to the surface was successful. Some irregularities in the latitudinal load dispersion onto the ski may occur when the weight guide is lowered. The irregularities can be caused by instabilities in the supports holding the weight guide. With this potential error in mind, it is possible that the variation in latitudinal pressure causes an uncertainty in the final measurements.

Chapter 4

Sensors

Chapter abstract: *This chapter investigates the functions of pressure-sensitive film sensors thoroughly. The basic functionality and construction of pressure-sensitive films are explained. The first section explains in detail how the conductive material of the sensor is manufactured and how the sensor registers force. Two types of sensors have been considered for this Master Thesis. The FlexiForce A201 pressure-sensitive film and Interlink 402 Force Sensing Resistor are compared and evaluated based on previous research conducted by Vecchi et al. (2000). The last part consists of a time-drift and linearity test to evaluate and confirm the linearity and characteristics of the FlexiForce A201 sensor. Although this chapter is technical, it is essential to understand how the sensor behaves under load to collect usable data from the sensor.*

4.1 Pressure-sensitive films

Pressure-sensitive films are thin sensors used to measure forces in areas where space is an issue. Thin-film sensors are seen in areas where one would need to register changes in forces to a solid or flexible surface. These force sensing sensors are also referred to as Force Sensing Resistors (FSR). Pressure-sensitive films and force-sensing resistors are sensors whose resistance decrease, i.e., conductivity increase, with increasing applied force.

4.1.1 Construction of the sensor

The sensor is typically based on five layers. As shown in Figure 4.1, the two out of five layers are protective films, which envelopes the sensor to protect the electrodes. In between the protective layers, two conductive electrodes encloses a layer of conductive ink. The electrodes allow electrons to flow

through the ink from one electrode to the other.

4.1.2 Construction materials

The electrodes consist of a conductive material like silver. Film materials used as protective layers, such as dielectric polyester, are elastic and flexible to allow placement of the sensor in various areas such as gloves for human-touch sensing and flat structures for sensing loads. The flexible material also works as an insulator for the electrodes. The ink used to conduct electrons between the electrode plates is described in Fraden (2005) to be produced by screen printing piezoresistive ink with a predefined pattern. The ink is printed as films having a thickness ranging from 10 μm to 40 μm. The ink is later dried at 150 °C and then sintered from 700 °C to 900 °C (Fraden 2005). The sintering makes grains of conductive and insulating oxides bind together and give them cohesion and strength, resulting in the ink containing small submicron particles of various metal oxides (Fraden 2005, 10.3, p.418).

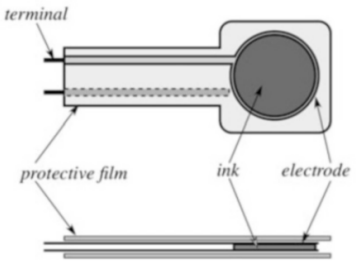

Figure 4.1: Composition of thin-film pressure sensor. Figure taken from Fraden 2005, p.418.

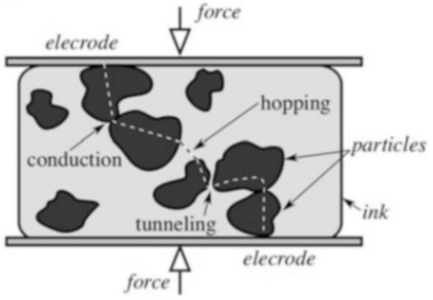

Figure 4.2: Concept of pressure-sensitive ink. Figure taken from Fraden 2005, p.418.

4.1.3 How does the sensor register force?

When applying force to the sensor, the conductivity between the electrodes is increased by three main mechanisms; conduction, hopping, and tunneling. Based on these three mechanisms, the amount of electrons passing through the ink increases with more force on the sensor. As shown in Figure 4.2, conduction is direct contact in the particles of the ink; this happens when the particles are fully connected. Hopping occurs when the particles are close enough to allow the electrons to jump. Typically, the jumping effect happens when the distance between the particles is around 10 nm. Tunneling happens

when the particles are barely touching (ca. 1 nm) and establishes a path for the electrons (Fraden 2005, 10.3, p.418).

4.1.4 Usage

The sensor operates in the voltage area of the input voltage of the circuit, ranging from 0 V to +5 V. By applying force on the sensor, the resistance decreases, and conductivity increases. Depending on the applied force on the sensor, the voltage output varies, allowing simple reading and measuring of the output voltage. The sensor's idle state, without load, is described to have mega-ohms of resistance, which makes the idle state challenging to read due to variations and uncertainties in the resistance. The circuits used with the sensors are typically simple voltage dividers or operational amplifier circuits. The latter prevents the sensor from drawing power directly from the circuit supply voltage resulting in more accurate readings.

4.2 FlexiForce A201 Sensor

The FlexiForce A201 sensor from Tekscan shown in Figure 4.3 is a pressure-sensitive film, constructed of two layers of plastic substrates films like polyester. Each layer consists of a conductive material (silver), which encloses a layer of conductive ink with adhesive (as described in Section 4.1.2). The sensing area is defined by a circular pattern of 9.53 mm, extended to two connectors for reading voltage. Tekscan, Inc. offers three variations of the FlexiForce A201 sensor shown Figure 4.3. LOW 4.4 N, MEDIUM 111 N, and HIGH 445 N, where the latter can be adjusted to have a sensing area up to 4448 N by adjusting the sensitivity in the circuit (Tekscan, Inc. 2019). Adjusting the sensitivity is explained later in Chapter 5.

4.3 Alternative sensors

Alternative sensors, like FSR sensor from Interlink Electronics, can be used. It is a conventional device used for sensing changes in force from contact, with an optimized sensitivity for use in human touch (Interlink Electronics 2019). The FSR sensor consists of two conductive layers with interdigitated patterns, which is commonly found in heat sensors. The interdigitated layers are deposited on a thermoplastic sheet facing a conductive polyetherimide film sheet. A spacer placed between the sheets allows electrical contact when force is applied (Vecchi et al. 2000). Similar to the Flexiforce A201 sensor,

the FSR-402 sensor shown in Figure Figure 4.4 is constructed with a circular sensing area with a diameter of 14.7 mm. Due to the size of the sensing area of the FSR-402 sensor, this sensor is not used in this thesis.

Figure 4.3: Force sensing sensor by Tekscan, Inc. Figure taken from Tekscan, Inc. (2019).

Figure 4.4: Force sensing resistor FSR-402 by Interlink Electronics. Figure taken from Interlink Electronics (2019).

4.4 Chapter results

Two tests were conducted on the FlexiForce A201 sensors. The first test was the time-drift test seen in Figure 4.5, to confirm the stability characteristics of the sensor, which was researched by Vecchi et al. (2000). This test was conducted using weights of 1500 g to load the sensor over five minutes. The results from the time-drift test show a drastic increase in conductivity of the sensor after approximately 65 seconds, thus reducing the output voltage. The reason behind the drop in output voltage instead of an increase in the output voltage is based on the circuit choice explained in Chapter 5. An area of stable output voltage was found between 14 and 32 seconds. The second test was the linearity test. This test was conducted with weight intervals illustrated in Figure 4.6. The weights were loaded in increased succession, to read the conductance value for each of the weights. The conductance output of the loaded weights are illustrated in Figures 4.7 and 4.8. By obtaining the linearity of the sensor, we could investigate the linear uncertainty of the output full scale provided by the manufacturer. The linearity error was calculated as Maximum Deviation σ_{max} from linearity with the formula:

$$\sigma_{max} = \max(\mid \vec{y}_{observed} - \vec{y}_{fitted} \mid). \tag{4.1}$$

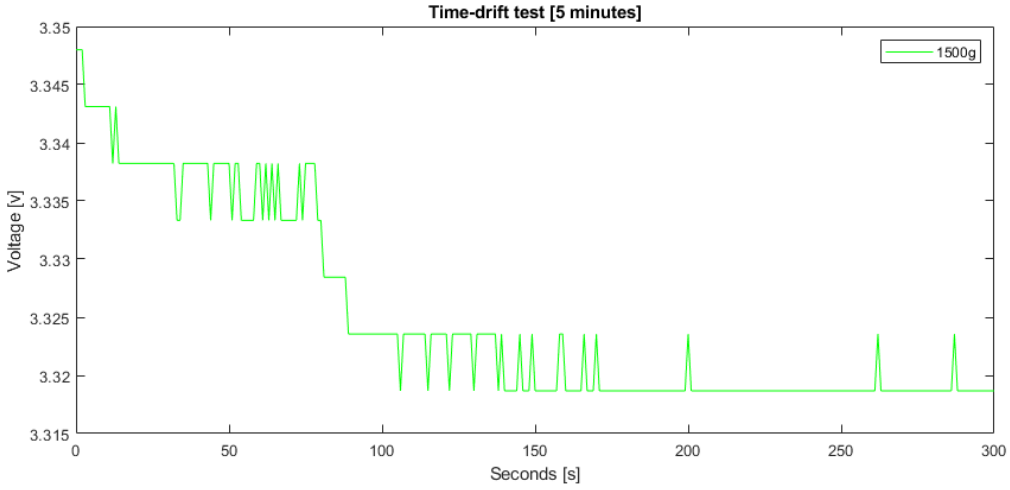

Figure 4.5: Time-drift test of the FlexiForce A201 sensor with 1500g load.

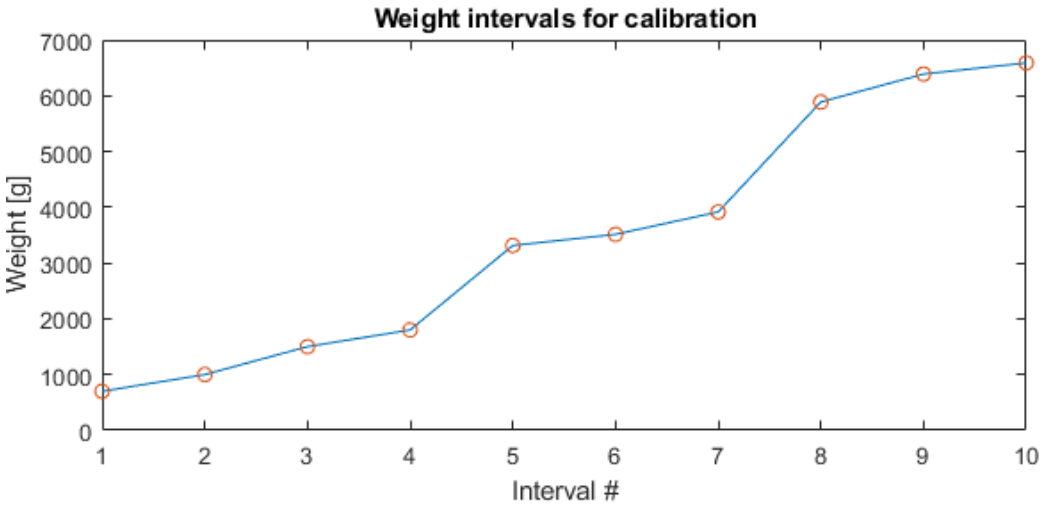

Figure 4.6: Weight interval for linearity test and sensor calibration.

The formula represents the worst case scenario of deviation in the measurement error. The maximum deviation for the first sensor tested seen in Figure 4.7, was calculated to be ±2.14 % and the second sensor seen in Figure 4.8 was calculated to ±3.95 %. Furthermore, inaccuracies in the range below 700 g was found and can be seen in Figure 4.9.

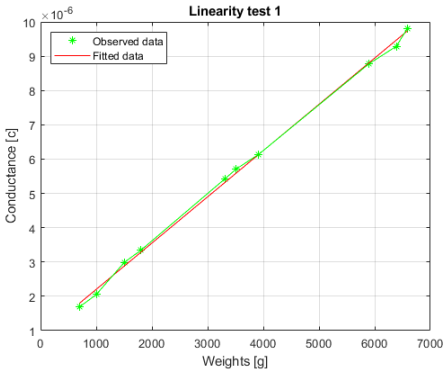

Figure 4.7: Linearity test 1 of FlexiForce A201 sensor.

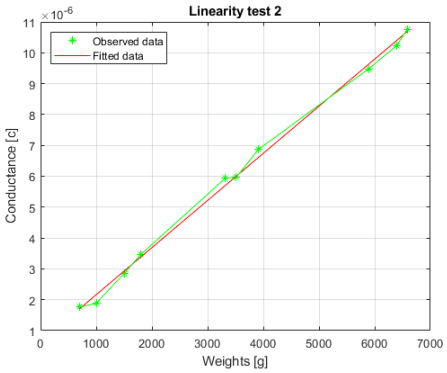

Figure 4.8: Linearity test 2 of FlexiForce A201 sensor.

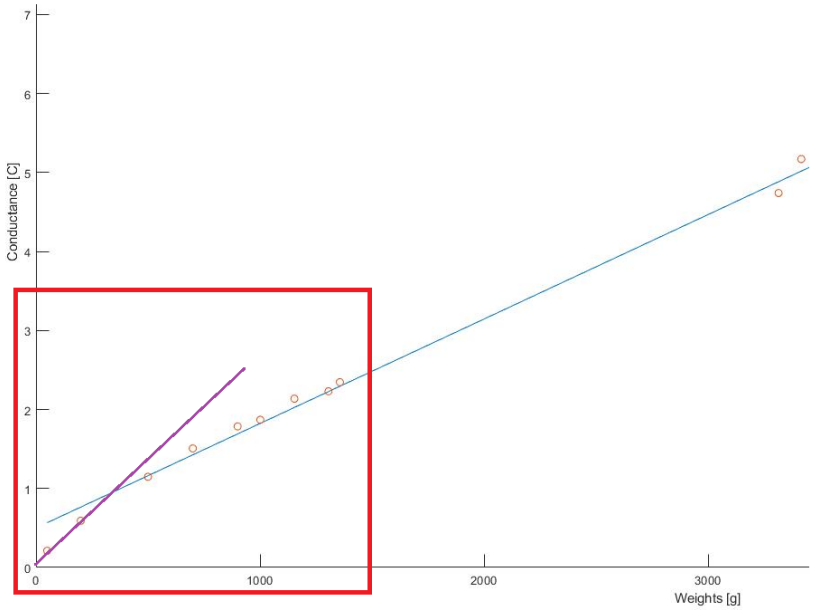

Figure 4.9: Figure illustrates non-linear results for weights below 700 g in terms of conductance versus force.

4.5 Chapter discussion and conclusion

Pressure-sensitive sensors are often linear in terms of conductivity versus force. Sensors like the FlexiForce A201 discussed in Section 4.2, has a linearity error provided by the manufacturer of ±3 % (Tekscan, Inc. 2019). The measurement quality investigated in the linearity test plotted in Figures 4.7 and 4.8, show errors of ±2.14 % and ±3.95 % in terms of linearity versus

force. Some of the linearity results from the tests match the specifications given by Tekscan, Inc. (2019), while the results showing an error beyond ±3 % can be caused by the time-drift characteristics presented in Section 4.4. Variations in the lower spectrum of the A201 sensor introduced an error beyond ±3 % linearity. A conclusion was made to discard measurement values below 700 g, and use these values to register contact.

The variation in the linearity error is a result of time-drift. This time-drift can be a result of the sintered ink in the FlexiForce sensor approaching a saturation state. Over time, the conductive material could be compressed to a state were the hopping mechanism shifts to tunneling mechanisms and tunneling shifts to the conduction mechanism for the submicron in the sintered ink. This shifting of mechanical states could increase the amount of current flow because of the increase in conductivity. Furthermore, the results from the time-drift test shown in Figure 4.5 tend towards non-linear after around 65 seconds, and the data is no longer usable. Allowing the ink to settle to ensure consistency in the results is essential when gathering data with the pressure-sensitive film sensors containing sintered ink as the conductive material (Vecchi et al. 2000). A window of stable output was found between 14 seconds and 32 seconds. This stable window illustrated in Figure 4.10 gives us an indication in which time window to conduct calibrations of the system described in Chapter 6, and to conduct measurements. The time-drift tests conducted by Vecchi et al. (2000) used a resting time of 30 seconds of the sensor between each trial. Our tests used heavier loads than the priory mention study. We found that letting the sensor rest for up to 60 seconds, gave more repeatable results in terms of output precision (i.e., the sensor's ability to produce repeatable results for each trial under the same measurement conditions (Pallas-Areny and Webster 2001)). Furthermore, Hollinger and Wanderley (2006) stated that force-sensing resistors like the Flexiforce sensor could not be used in quantitative or absolute measurements of force. We can agree with this statement to a certain extent if measurements over an extended period are necessary. For our case, the measurements are ideally conducted in the time window of 14 seconds to 32 seconds, and the FlexiForce sensor can, therefore, be used in quantitative measurements. The dimensions of the FSR sensor from Interlink Electronics did not meet the size requirements to be placed on a mechanical system described in Section 3. FlexiForces' A201 sensor allowed two sensors to fit under the width of a cross-country ski, thus giving the ability to conduct two-dimensional measurements of a cross-country ski. Based on the researched done by Vecchi et al. (2000), the same choice of sensors was made for this thesis after conducting the time-drift and linearity tests. The FlexiForce A201 sensor met the required specifications of linearity and force-limitations(0N - 245.25N). The

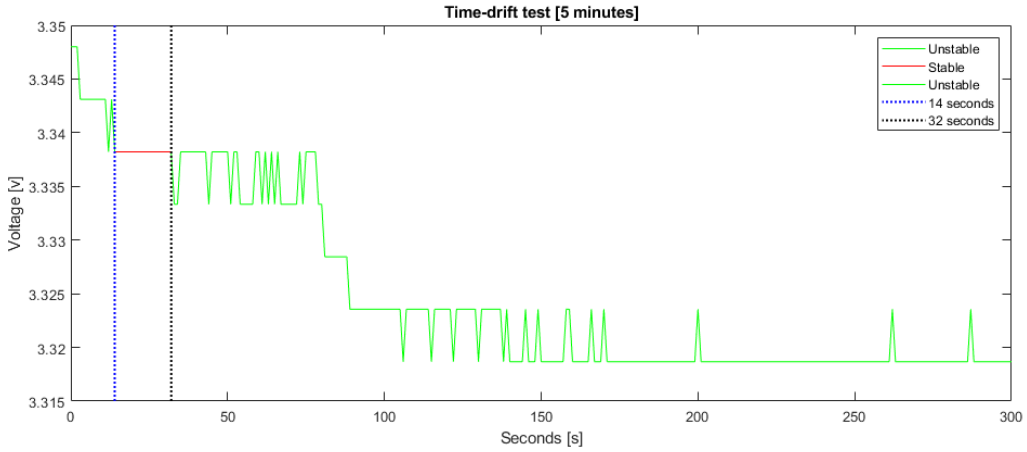

Figure 4.10: Stable measurement area, illustrated from the time-drift test.

sensor needs to handle a total loading weight of 25kg (245.25N), which was based on the sensor placement with the total loaded weight on the system. The mechanical design presented in Section 3, divides half the FBW loaded onto each side of the system along the longitudinal length. The weight was again divided between the two sensors along the latitudinal length of the system. Maximum possible load on a single sensor was therefore considered to be $FBW/4$.

Chapter 5

Circuits

Chapter abstract: *For measuring the response of a pressure-sensitive film, a circuit was formed to obtain stable and accurate measurements. This chapter investigates the characteristics of two types of circuits; a voltage divider circuit and two versions of an operational amplifier circuit. First off, we look at the simulation software used to simulate the operational amplifier circuit for voltage output behavior. Then, we analyze and adjust the sensitivity of the circuit to fit the required range of weights to be measured. The chapter is then finished off with looking at the assembling process of the circuits and a variance test to investigate the stability and measurement quality of the operational amplifier circuit output with FlexiForce A201 sensors.*

5.1 Voltage divider

The voltage divider shown in Figure 5.1 is one of the simplest forms of circuits used with a sensing element like a pressure-sensitive film. The quality of the measurement result is based on the voltage read from the circuit. The output voltage varies when the resistance of the sensor changes due to the applied force. This output voltage is based on the analytic formula:

$$V_{out} = V_{supply} \cdot \frac{R_1}{R_{flexiforce} + R_1}. \tag{5.1}$$

When applying pressure on the sensor, the resistance in the sensor decreases, resulting in an increase in value from the fraction in Equation 5.1. The output voltage V_{out} then increases as more pressure is applied. One of the benefits of using a voltage divider is easy implementation. On the contrary, we can experience more noise in the measured voltage and measurement spike due to the lack of capacitors. This type of circuit causes

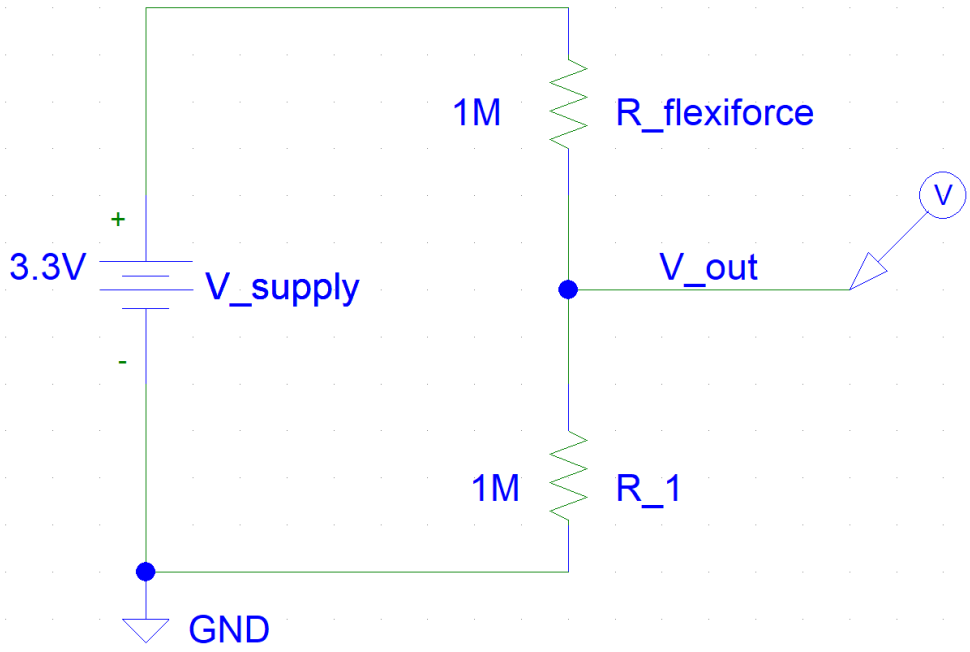

Figure 5.1: Voltage divider circuit for sensing changes in pressure sensitive films (created in PSpice).

the sensor to draw power straight from the power source supplying the circuit. The applied pressure can lead to current drops under initial loading of the sensor and during measurements. This current drop is a commonly observed phenomenon which can introduce inaccuracies in the voltage output. An operational amplifier circuit is beneficial when sensing elements like pressure-sensitive film are used.

5.2 Operational amplifier circuits

The operational amplifier is equipped with an external power source, from which the sensor draws power. Operational amplifiers are 3 terminal devices used to amplify voltages, two inputs and one output, with an addition of two power connections as V_{supply} to power the operational amplifier. The supply voltage decides the operational output voltage range of the amplifier. This operational output voltage range usually caps at $\pm 15V$, which gives an upper and lower limit of to how much the operational amplifier can amplify voltages. These operational amplifiers are described to have infinite input impedance,

meaning an infinite resistance on the two inputs, hindering current flow between the inputs. Operational amplifiers in real-world applications are never ideal. Operational amplifiers can be connected in two main forms of circuits, the *Inverting operational amplifier circuit* Section 5.2.1 and *Non-inverting operational amplifier circuit* Section 5.2.2. The gain A of an operational amplifier can be adjusted by increasing or decreasing the feedback or input resistance in the circuit (Fraden 2005).

5.2.1 Inverting Operational amplifier circuit

The inverting operational amplifier seen in Figure 5.2 is based on the characteristics described in Section 5.2. This circuit is based on a negative feedback connection of the two inputs available, meaning the output of the operational amplifier is connected back to the negative input. The negative feedback connection results in an amplified signal with a negative sign. In this case, the pressure-sensitive film $R_{flexiforce}$ is connected with the supply voltage V_{in} to the negative input pin. The output voltage V_{out} varies from $0V$ to down to $-V_{supply}$. However, alternatively, one can use a biased input. When using a biased input, the circuit can vary from V_{bias} down to $0V$ or the lowest value supplying the operational amplifier. When applying force to the sensor, resistance in the sensor $R_{flexiforce}$ decreases, and the voltage from V_{in} over the sensor increases. The voltage in the negative input pin is amplified by the feedback loop from the voltage output of the operational amplifier. The output voltage of an inverting operational amplifier can be derived from Kirchhoff's 2$^{\text{nd}}$ law which states that the sum of currents in a closed circuit equals zero:

$$I_{flexiforce} - I_{feedback} = 0, \tag{5.2}$$

i.e.,

$$I_{flexiforce} = I_{feedback}. \tag{5.3}$$

From Equation 5.3, currents over the components $I_{flexiforce}$ and $I_{feedback}$ can be rewritten with Ohm's law:

$$\frac{V_{in} - V_{bias}}{R_{flexiforce}} = \frac{V_{bias} - V_{out}}{R_{feedback}}, \tag{5.4}$$

and, with respect to V_{out}, we end up with:

$$V_{out} = (V_{bias} - V_{in})\frac{R_{feedback}}{R_{flexiforce}} + V_{bias}. \tag{5.5}$$

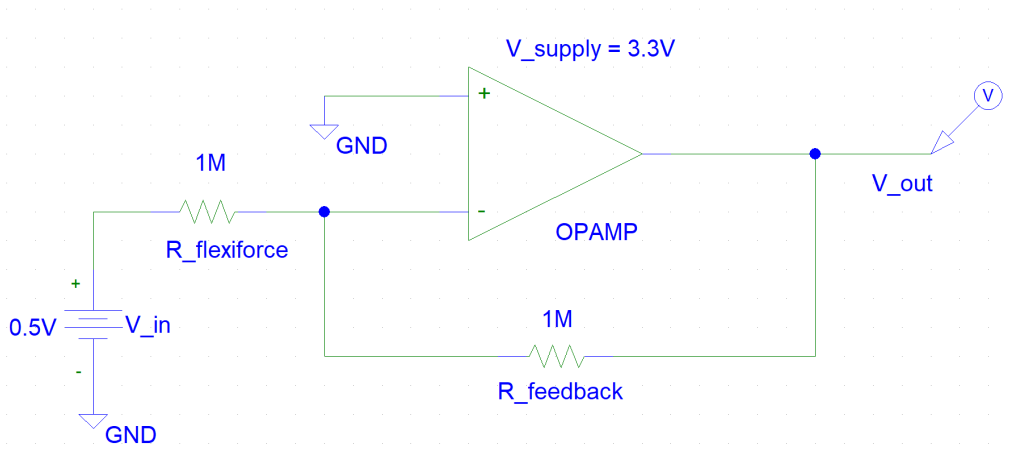

Figure 5.2: Example of unbiased inverting operational amplifier circuit for sensing changes in pressure sensitive films $R_{flexiforce}$, in unity state A=-1 (created in PSpice).

The amount of amplification in the circuit is decided by the relation between $R_{feedback}$ and $R_{flexiforce}$:

$$A = -\frac{R_{feedback}}{R_{flexiforce}}. \tag{5.6}$$

The negative sign come from the negative feedback loop and leads to rewriting Equation 5.5 for output voltage to:

$$V_{out} = -(V_{bias} - V_{in})A + V_{bias}. \tag{5.7}$$

Unity state is defined were $R_{feedback}$ and $R_{flexiforce}$ are equal (Fraden 2005).

5.2.2 Non-inverting operational amplifier circuit

Much like the inverting operational amplifier, the non-inverting version (positive feedback) connects its feedback loop to the positive input on the component. In addition to the positive feedback loop, the feedback also runs to ground shown in Figure 5.3. The effect of using a non-inverting operational amplifier circuit is an overall increase in gain compared to the inverting operational amplifier circuit. Again, V_{out} of a non-inverting operational amplifier

circuit can be derived from Kirchhoff's 2nd law. From Equation 5.3 we get:

$$\frac{V_{in}}{R_{flexiforce}} = \frac{V_{out} - V_0}{R_{feedback}}, \tag{5.8}$$

were V_0 is the virtual ground in the divider between $R_{feedback}$ and $R_{flexiforce}$. The potential difference over the two inputs of the operational amplifier give us $V_0 = V_{in}$:

$$\frac{V_{in}}{R_{flexiforce}} = \frac{V_{out}}{R_{feedback}} - \frac{V_{in}}{R_{feedback}}. \tag{5.9}$$

With respect to V_{out} we can derive:

$$\frac{V_{out}}{R_{feedback}} = \frac{V_{in}}{R_{flexiforce}} + \frac{V_{in}}{R_{feedback}}$$

i.e.,

$$V_{out} = R_{feedback} V_{in} (\frac{1}{R_{flexiforce}} + \frac{1}{R_{feedback}}). \tag{5.10}$$

From Equation 5.10, we end up with:

$$V_{out} = V_{in} (\frac{R_{feedback}}{R_{flexiforce}} + 1). \tag{5.11}$$

The gain A for non-inverting operational amplifier circuit is found with:

$$A = \frac{R_{feedback}}{R_{flexiforce}} + 1. \tag{5.12}$$

Inverting operational amplifier circuit is used over the non-inverting amplifier circuit due to the overall amplification increase in the latter circuit. Refer to Equation 5.6 and Equation 5.12 for comparison.

5.3 Simulating the circuits

The simulation of the circuits was an essential step in designing and tuning the circuits. It was first and foremost important to look at the behavior of the circuit under the ideal condition to understand how they would perform in terms of the output voltage. By simulating the circuits, the appropriate resistance values for the feedback resistor could be found. PSpice was the first simulation program for initial tests of functionality, LTSpice was later used for more in-depth investigation of output full scale responses with different size of feedback resistors.

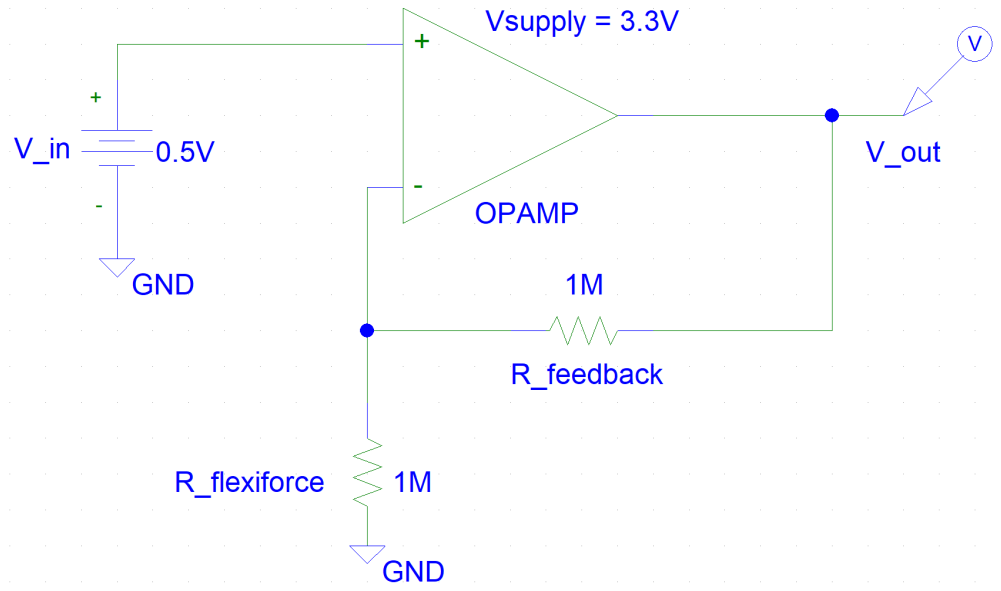

Figure 5.3: Example a non-inverting operational amplifier circuit for sensing changes in pressure sensitive films $R_{flexiforce}$, in unity state A=2 (created in PSpice).

5.3.1 PSpice Design Manager

PSpice Design Manager version 9.1 is an older version of the PSpice software line developed by OrCad™. Version 9.1 was available for free by the University of Oslo and is the reason for using this version. PSpice Design Manager was used early in the design process for designing the circuits. The program allows you to place ideal components to investigate currents and voltages for ideal conditions.

5.3.2 LTSpice

LTspice® is a SPICE simulation software developed by Analog Devices. LTspice® offers in-depth analysis of circuit behavior. This program was used to decide the $R_{feedback}$ and capacitors. Figure 5.4 show a simulated inverting operation amplifier circuit. More detailed investigation of $R_{feedback}$ is explained in Section 5.4.

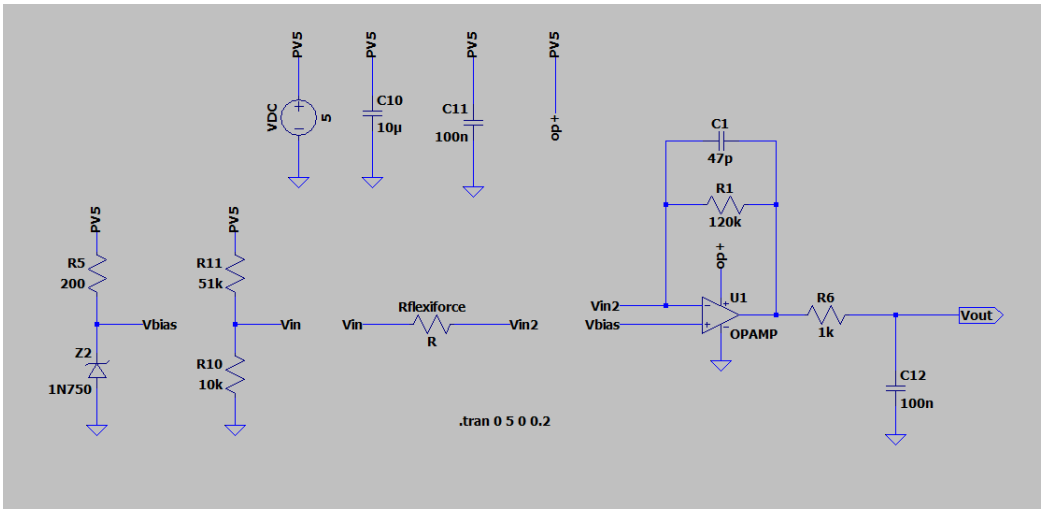

Figure 5.4: Simulation of inverting operation amplifier circuit in LTspice®.

5.4 Choosing the right feedback resistor

Adjusting the sensitivity of the inverting operational amplifier circuit (i.e., how fast the operational amplifier saturates to $0V$ with increasing weights) results in which range of forces we get more precision in the voltage output from the FlexiForce A201 sensor. When determining the size of $R_{feedback}$, we consider two criteria; 1. at which weight do we want the most accuracy (i.e., when the operational amplifier is in unity gain $R_{feedback} = R_{flexiforce}$), and 2. what our upper limit of measurable force should be. Investigating cross-country skis in a gliding phase equals the maximum force on one sensor to $HBW/4$; for this, we used an example of 45 kg as the HBW. The resistance value of the sensor at 45 $kg/4 = 11.25$ kg was measured with a multimeter and set as the upper limit of measurable force. Using the analysis plot shown in Figure 5.5, the saturation value of 0 V was equal to 10 kg for a $R_{feedback}$ value of 140 $k\Omega$. The unity gain was wanted to be at around 4 kg were most of the pressure was anticipated to be. A choice was made for the $R_{feedback}$ to be at 180 $k\Omega$ were the upper limit of measurable forces was around $7-8$ kg and unity gain at around 3.2 kg. The output voltage at the unit gain weight is found with Equation 5.7, with $A = 1$.

$$V_{out} = (V_{bias} - V_{in}) + V_{bias} = 3.88 - 5 + 3.88 = 2.77 \tag{5.13}$$

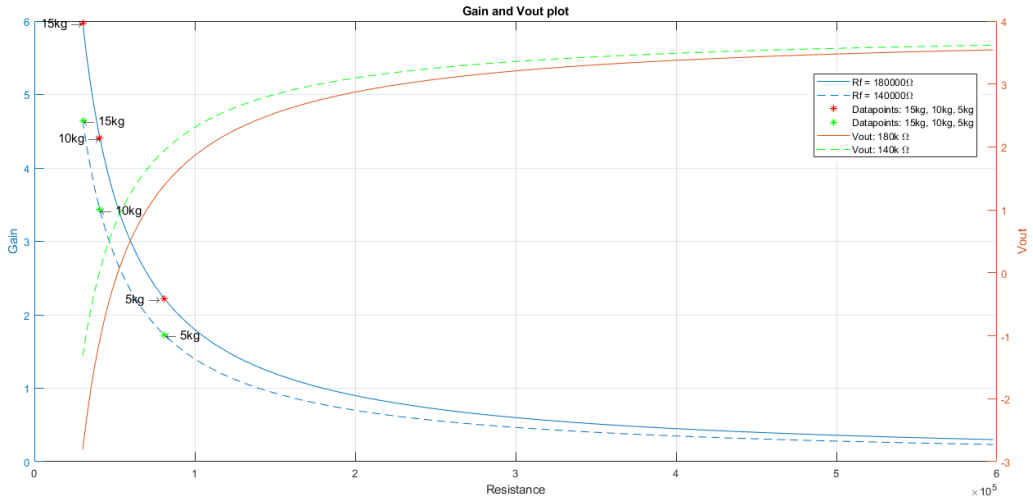

Figure 5.5: Analysis for choosing the right $R_{feedback}$. Investigation of maximum load before operational amplifier saturation.

5.5 Assembling the circuits

After analysis of the components and simulation of the circuits were completed, constructing of the circuits remained. Consultation with the Electronics-Lab (E-Lab) at the University of Oslo, Department of Physics presented the opportunity to borrow the electronics lab for circuit construction. The circuit boards were designed based on simulations and components analyzed in this chapter. The experienced personnel at E-Lab helped etch out the design of the circuit boards for installation of 1206 ($3.2\ mm\ x\ 1.6\ mm$) sized components. The surface-mounted components were installed with the help of a Fritsch LM901 manual pick and place device (Fritsch GmbH 2019). The components were placed on top of soldering paste to be soldered in a heated soldering oven. The component installation is shown in Figure 5.6. A total of 12 circuits, with the capacity of holding four sensors each, were produced for implementation in the mechanical system. Finished circuit designs are presented in Appendix 9.1.

5.6 Chapter results

A variance test was conducted on a biased inverting operational amplifier circuit using an Arduino UNO microcontroller explained in Chapter 6. The variance test was used to investigate the variance in the output voltage on the FlexiForce A201 sensor during idle, and weights of 1500 g and 3315 g. Each

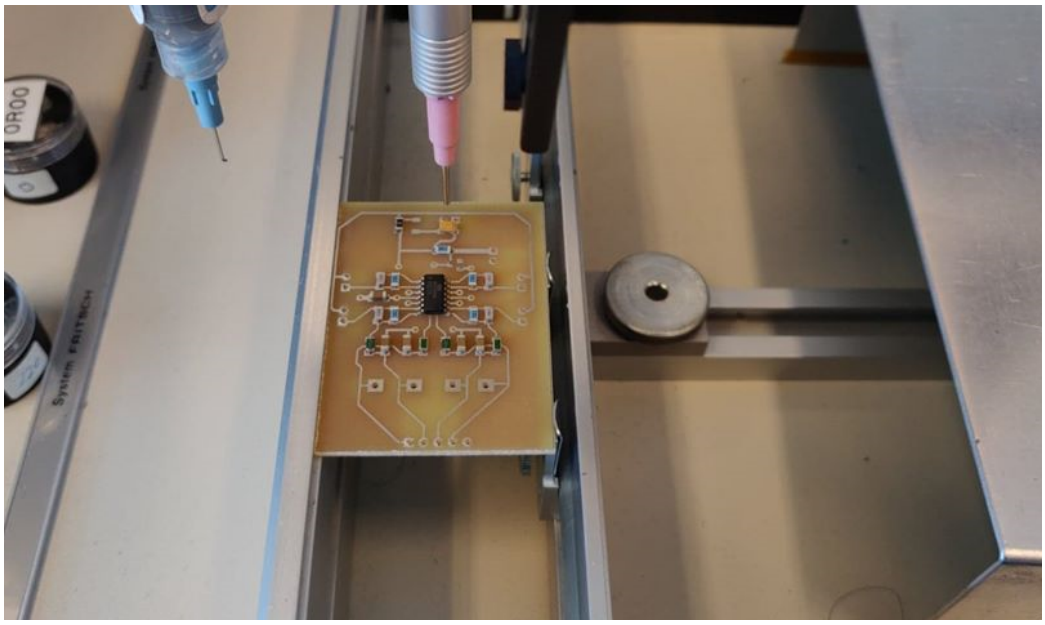

Figure 5.6: Placement of 1206 (3.2 mm x 1.6 mm) sized surface-mount components with Fritsch LM901 pick and place device.

test trial consisted of 100 samples and is presented in Figures 5.7, 5.8, and 5.9. The results of the variance test are shown in Table 5.1. Furthermore, the power consumption of the circuits was measured. The power from standard USB 2.0 ports are limited up to 0.5 ampere (500 mA) at 5 V (He 2015). The measured power consumption was 5 mA per circuit, which resulted in 60 mA for all 12 circuits.

Weight (g)	**Voltage mean** (μ)	**Standard deviation** (σ)	**Variance** (σ^2)
No load	3.9491	0.0012	$1.4381 \cdot 10^{-6}$
1500	3.3328	0.0026	$6.5150 \cdot 10^{-6}$
3315	2.7825	0.0023	$5.0673 \cdot 10^{-6}$

Table 5.1: Statistics from the variance test of FlexiForce A201 sensor.

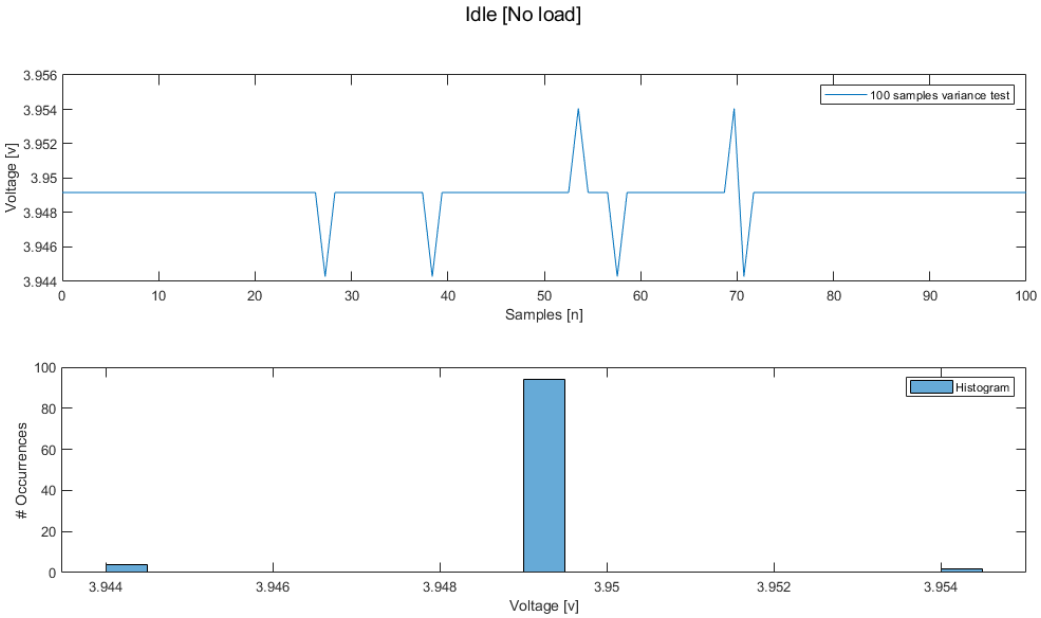

Figure 5.7: Variance test of 100 samples, no weight.

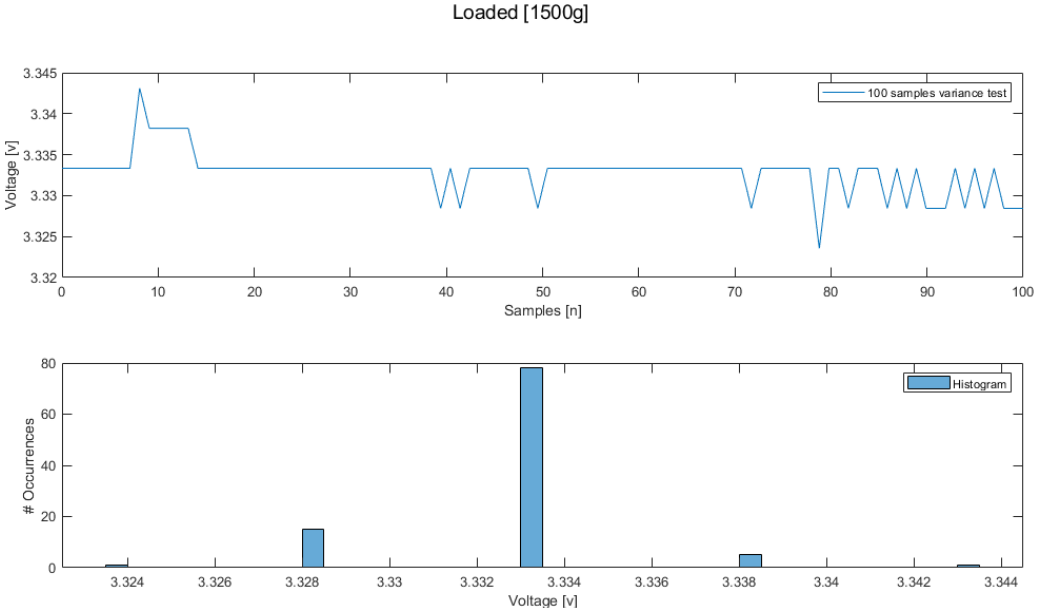

Figure 5.8: Variance test of 100 samples, 1500g weight.

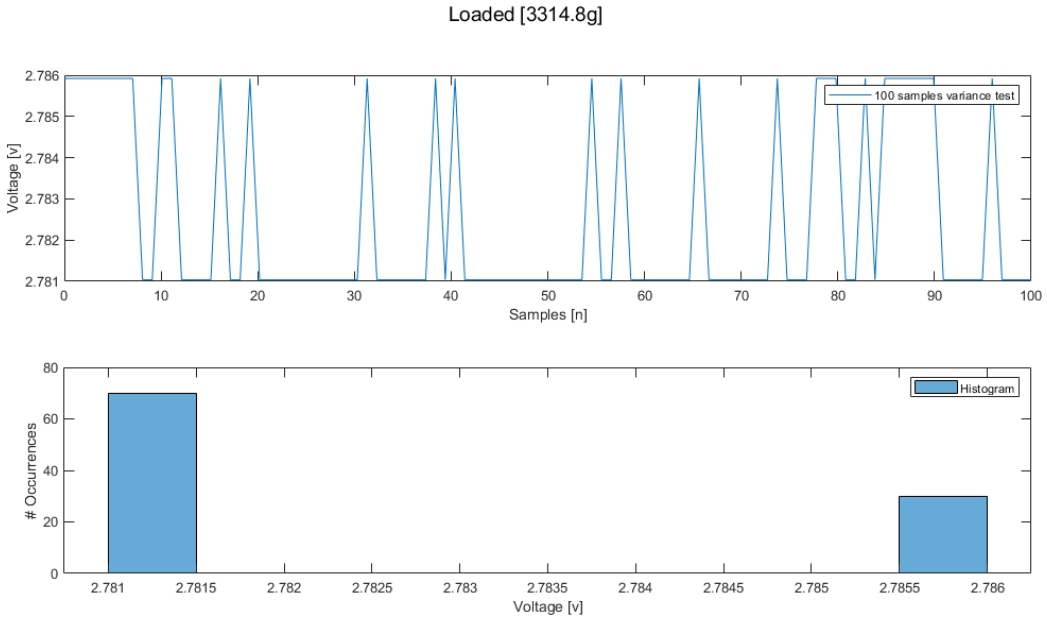

Figure 5.9: Variance test of 100 samples, 3315g weight.

5.7 Chapter discussion and conclusion

A biased inverting operational amplifier circuit was selected with low-noise outputs and low-power consumption, where Tekscan, Inc. (2019) suggested a inverting operation amplifier circuit. A biased version shifted the output full scale from 0 $V \rightarrow -V_{ref}$ to $+V_{ref} \rightarrow 0$ V, which prevented the use of negative supply voltages. Additionally, the Arduino UNO microcontroller was not able to measure negative input voltages. The results presented in Figure 5.5 show non-linear results in terms of resistance versus force. The circuit characteristics show that forces in the higher spectrum of voltage output (3.98 $V \rightarrow 3$ V) have less resolution compared to the lower spectrum. The amount of change in output voltage per resistance is significantly lower compared to the output voltages lower than 3 V. This low resolution, in combination with the analog-to-digital converter (ADC) in the Arduino UNO, can be a source of ADC reading errors. The ADC resolution and reading errors are explained in detail in Section 6.3. The variance test presented in Tabel 5.1 shows lower variance closer to unity gain of the operational amplifier, which was expected. The unity gain was found to be around 3.2 kg or 2.77 V, see Section 5.4. After testing all 12 circuits for flaws and production errors, the circuits were placed in the mechanical system for handling stable output voltages for digital measurements explained in Chapter 6.

Chapter 6

Digital measurements

Chapter abstract: *The following chapter investigates the required elements of conducting digital measurements from the mechanical system. First, we discuss what microcontroller units are and what components they are made of. Secondly, the concepts of analog-to-digital converters are explained since they have a high impact on the precision of what is measured. A quick overlook of the software that was used to develop algorithms and tools to conduct and analyze the measured data are shown. For the final part of the chapter, we discuss different calibration methods, and we calibrate the system. The results of calibrations are analyzed and discussed further to give the reader a better understanding of the importance of calibration.*

6.1 Microcontroller units

Microcontroller units (MCUs) are small programmable computers used to control input and output gates. An MCU contains one or more central processor units (CPUs), where the speed of the CPU is often used as a measurement for quality and speed of the MCU. The speed or capacity of the CPU is measured in Hertz (Hz) and is the rate of how many operations it can handle per second. MCUs may contain one or more analog-to-digital converters (ADC) to convert analog signals to digital signals. The conversion is done by the ADC with sample-and-hold techniques to produce a digital signal from the varying input to a series of bit values (Analog Devices 2009). The accuracy of an ADC is affected by the bit size of the ADC. Bit size translates to how many quantizations steps the ADC can convert and is referred to as resolution. For each sample in milliseconds, a bit value is assigned related to the level on the varying signal. A faster CPU will sample more often, but may not register changes in the signal if the resolution is poor as seen in

Figure 6.1. Small errors in the conversions from an ADC are unavoidable, thus choosing a higher bit ADC with more quantization steps will often be more beneficial to detect smaller variations in the varying signal.

6.1.1 Arduino Uno Rev3

Arduino Uno Rev3 shown in Figure 6.2, is a microcontroller board produced by Arduino® and is based on the ATmega328P 16 MHz CPU. The unit offers 14 digital input/output pins and six analog inputs. Arduino Uno Rev3 is either powered through a universal serial bus (USB) or an external battery source, where the USB connection allows for the transfer of C++ code to the board through Arduino Software (Arduino AG 2019). The board has one 10 bit ADC built-in, and the board supports an external multiplexer board like the MUX Shield II for extending the number of input/output pins from 3 of the analog inputs on the MCU to 48 on the MUX Shield II with 3 channels of 12 inputs (Mayhew Labs 2019). The multiplexer on the Arduino board uses a truth table to determine the input/output gate to sample. While using the MUX Shield II, the Arduino Uno Rev3 uses a combination of two multiplexers; the built-in ADC for choosing one of three channels on $A0$, $A1$ or $A2$, and a second multiplexer from the MUX board which uses selector values or truth table to choose one input between 1 and 12. The result is a combination of 48 different analog inputs or digital output/input. For one ADC, the MUX Shield II introduces a much higher workload on the CPU in the MCU, which has to sample the 48 inputs/outputs on every cycle. The board has a reference voltage pin V_{ref} which allows for adjustment of the voltage operating range of the ADC. The default setting for V_{ref} is set to $5\,V$, which makes the ADC allocate its resolution over this voltage range. By adjusting the V_{ref} to a lower voltage value, the resolution can be distributed over a lower voltage range for each specific application area.

6.2 Software

This section takes a look at the MATLAB® environment and different toolboxes used to develop algorithms to do digital measurements from the mechanical system. Developing the algorithms is the last step to complete a functioning mechanical system to read and analyze the data from load sensors.

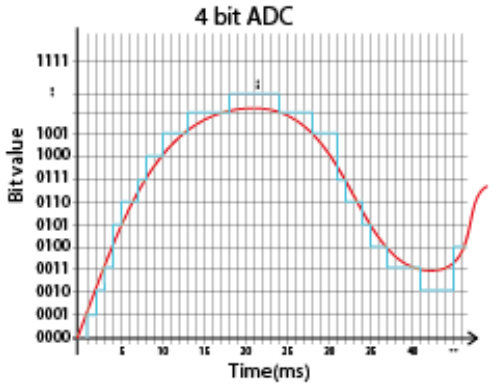

Figure 6.1: Concept of analog-to-digital conversion in a 4 bit ADC.

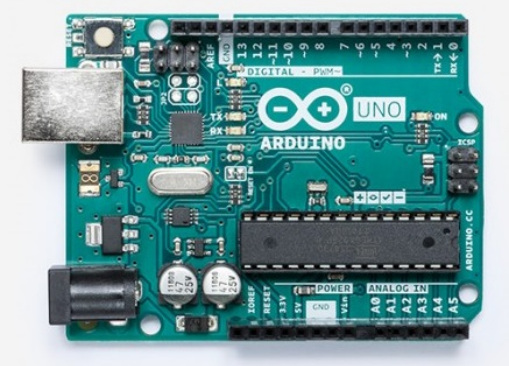

Figure 6.2: Arduino Uno Rev3 MCU. Figure taken from Arduino AG (2019).

6.2.1 MATLAB

MATLAB® is an environment for analysis and calculations of mathematical matrices and arrays, using the programming language to develop algorithms to complete iterative tasks (MathWorks 2019). The environment uses toolbox kits with known algorithms for eased use. Toolboxes, such as the *MATLAB Support Package for Arduino Hardware*, allows MATLAB® to establish a connection to the Arduino Uno Rev3 board for a live reading and data analysis. Algorithms can then be developed to read each of the input gates on the Arduino board for analyzing load data from the sensor. All MATLAB® algorithms developed for this thesis project are presented in Appendix 9.1.

6.3 Calibrating the mechanical system

Multiple methods can be applied for calibrating the mechanical system. This section investigates two calibration methods, which adjust the measured values outputted by the load sensors. Much like a temperature sensor, a load sensor needs a scale for the software to calculate correct load values based on the output voltage of the circuit. The measured values sampled by the MCU and software has no relevance to load in the absence of a scale, either being an absolute scale or a relative scale.

6.3.1 Calibration methods

Calibration methods for load sensors vary for different application areas. One method requires physical modifications of the sensor to reduce the size of the

sensing area, while another method modifies the values read by the system through software.

Modifying the physical properties of the sensor

An alternative way of calibrating the sensor is to modify the properties of the sensor physically. These physical modifications can be trimming the size of the sensors or removing portions of the sensing areas to reduce the contact zone, which is irreversible in a sense that it damages the fundamental properties of the sensor. The physical modifications not only do permanent damage to the sensor, but it also makes it significantly harder to adjust for environmental changes over time. The environmental changes can be tear damage, aging of the materials used in the sensor, and change in temperature (Fraden 2005). For a pressure-sensitive film or load sensor using ink as the conductive material, adjusting the physical modifications would most likely introduce errors in linearity due to interference in the conductivity. Therefore, this calibration method was not applied in this thesis.

Modifying the full-scale output

The full-scale output (FS) is the relation between the input stimulus s and the output response. The full-scale output defines the minimum and maximum value the system can output with a given stimulus. Essentially, the full-scale output is the measured output voltage from the measurement system and can be modified when reading the output voltage. This calibration method can typically be to create a system response, which can be a regression line fitting model between a minimum and maximum value. The regression line fitting model used in this thesis is based on a first-degree *polynomial regression* of the following general polynomial regression model:

$$y = \beta_0 + \beta_1 x + \beta_2 x^2 + \cdots + \beta_n x^n + \epsilon. \tag{6.1}$$

The first-degree polynomial regression is a straight non-vertical line that models the expected value from the observed data with least square estimation. For the FlexiForce A201 sensor used in this thesis, the observed values are the sensors output in terms of resistance from each of the calibration weights, which will be described later in this section.

6.3.2 Calibration weights

Calibration of the sensors and the mechanical system requires a relative scale for comparing resistance values of the sensor to the relative weight or force.

The weights chosen for this task is shown in Figure 4.6, which was also used to test the linearity of the sensors in Chapter 4. The weights increased in a somewhat linear fashion spread across the expected full-scale output of the sensor.

6.4 Chapter results

The circuits with sensors attached were spread out along the longitudinal and latitudinal length of the mechanical system. The two columns along the longitudinal length were defined as channel 1 and channel 2 for indexing the sensors y-location. The channel and sensor setup is illustrated in Figure 6.3. For indexing the sensors x-location, 24 sensors were placed in each column to a total of 48 sensors. The first index was set for sensor 1 placed toward the tip of the ski, while sensor 24 was the last sensor placed towards the back end of the ski. The sensor placement created a 2 x 24 array of sensors. The first trial of the calibrations conducted was for each of the 12

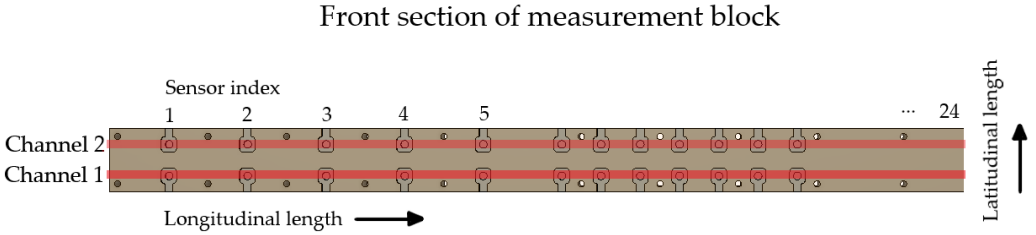

Figure 6.3: Illustration of channels and sensor index setup.

circuits. For each circuit, a system response was created for two arbitrary sensors with the calibration weights from Figure 4.6. Circuit-specific calibrations were conducted to cancel out the variations in each circuit. While creating system responses for sensors, a measurement of the output voltages for each weight was required. The resistance value of the sensor was then found with Equation 5.7 for $R_{flexiforce}$ for each of the weights in the weight interval. The resistance values were then inverted to find the conductance values $c_{flexiforce}$. First-Degree polynomial regression was applied to create a non-vertical approximation line to fit the measured conductance values best, as shown in Figures 6.4 and 6.5. The two system responses were then averaged to create a mean system response for each specific circuit shown in Figure 6.6. The circuit calibration method resulted in significant variations in the output voltages for all four sensors on each circuit.

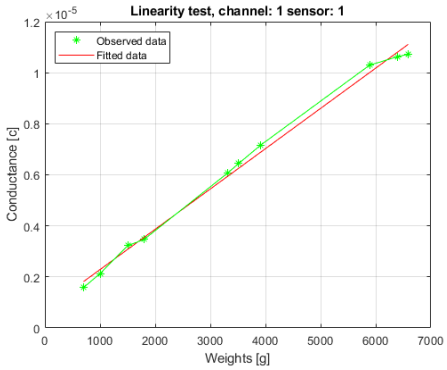

Figure 6.4: Linearity test of calibration; channel 1, sensor 1.

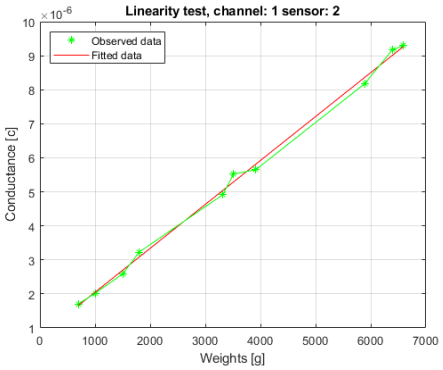

Figure 6.5: Linearity test of calibration; channel 1, sensor 2.

A second trial of calibrations was focused on sensor specific calibration. As in circuit-specific calibration, the first-degree polynomial approach was used to create system functions for all sensors. For each sensor, the resistance values were collected and inverted. The system functions for each sensor seen in Appendix 9.1, resulted in reduced maximum deviation error from linearity for each sensor compared to circuit-specific calibration. Table 6.4 show the maximum deviation error from linearity of an excerpt of all the sensor calibrations presented in Table 9.1.

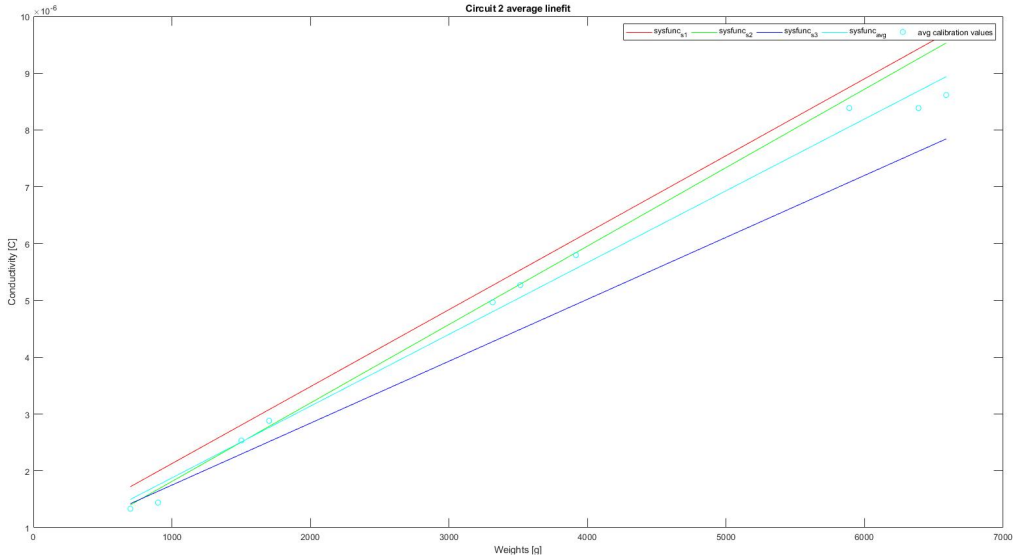

Figure 6.6: Figure illustrates the average system function based on three sensors for circuit 2.

Channel	**Sensor**	**Maximum deviation (%)**	**Maximum deviation**
1	*1*	3.4619	$3.8464 \cdot 10^{-7}$
1	*2*	4.2950	$2.2744 \cdot 10^{-7}$
1	*3*	4.8202	$7.4252 \cdot 10^{-8}$
1	*4*	1.9057	$1.8048 \cdot 10^{-7}$
1	*5*	12.8473	$2.7818 \cdot 10^{-7}$
2	*6*	5.2083	$6.5310 \cdot 10^{-7}$
2	*7*	5.9676	$7.3503 \cdot 10^{-7}$
2	*8*	5.3405	$5.4219 \cdot 10^{-7}$
2	*9*	4.0102	$3.5472 \cdot 10^{-7}$
2	*10*	10.2433	$2.7871 \cdot 10^{-7}$

Table 6.1: Maximum deviation from linearity calculations in terms of conductivity versus force. An excerpt of Table 9.1 in Appendix 9.1.

6.5 Chapter discussion and conclusion

The goal of calibrating the mechanical system was to investigate the variation in maximum deviation error from linearity for different methods. The circuit-specific calibrations were done to investigate if the variations in the circuits were the more significant factor for measurement errors. The difference between the two system functions used to create the mean system functions was too significant. Therefore, the decision was made to conduct sensor-specific calibration. This calibration process was more time-consuming but resulted in less error and more precise results in terms of load representation. The results presented in Figure 6.4, consists of some error anomalies. Some of the calibrations performed were not accurate enough because of the sensor's time-drift characteristics. Some of the conductance values may have been collected outside the stable area of the sensor discussed in Chapter 4. Another thing to consider is that the error calculated is relative to the placement of the value in the full-scale output. A small error in the lower spectrum closer to 700 g will give a more significant error percentage than an equally small error higher up the spectrum. Some calibration values with the maximum deviation in the lower spectrum can explain the error anomalies in Tables 9.1.

Chapter 7

Results

Chapter abstract: *This chapter presents the measurement results of four classical cross-country skis. The skis measured was one pair of cold skis/All-round skis (Fischer Speedmax Classic Plus 812) and one pair of warm skis (Fischer Speedmax Classic Plus 902). The skis were borrowed from Milsluker'n Ullvål in Oslo, and the skis are described in the first part of the chapter. Methodical tests are conducted to prove repeatability and accuracy of the mechanical system. An attempt on creating ski profiles and pressure distribution plots is made.*

7.1 Fischer Speedmax Classic Plus 812

Speedmax Classic Plus 812 is a classical racing ski developed by Fischer for cold weather and snow conditions. As described by Milsluker'n (2019), the 812 ski construction is suited as an all-round ski with extended pressure zones (i.e., longer contact area). The 812 ski pair was labeled 812_1 and 812_2.

7.2 Fischer Speedmax Classic Plus 902

Speedmax Classic Plus 902 is a classical racing ski based on the 902 construction by Fischer. The 902 ski have higher load zones closer to the camber pocket in both front and back section which allows the camber pocket to "open up". This allows for more gripping wax typically used for warm weather and snow conditions (Oslo Sportslager 2019). The 902 ski pair was labeled 902_1 and 902_2.

7.3 Ski measurements

The ski measurement process consisted of ten measurement cycles. Each of the four skis was measured once per measurement cycle, for a total of ten measurements per ski. A total of 40.6 kg (i.e., approximately the skis stiffness characteristics for HBW) was placed on the linear weight guide to transfer the load on the binding point. The skis were loaded by lowering the handle on the linear weight guide as seen in Figure 7.1. The sensors laying underneath the skis are picking up the load on each sensor location from the skis running surface. The ski is under consistent load for 15 seconds to approach the stable area in terms of time-drift to ensure more accurate measurements (see Section 4.5). After 15 seconds, the MATLAB® algorithm created (see Appendix 9.1), starts sampling all the channels on Arduino MCU twice for averaging. As mentioned in Chapter 6, the resistance value of all the sensors is calculated and inverted. By plugging the conductance value of a sensor into the belonging system function, a load representation is calculated (see Appendix 9.1 for calibration values and system functions). The load representation is then arranged into a two-dimensional array to represent the left side (channel 1), and the right side (channel 2) of the skis. This two-dimensional array gives us the pressure distribution.

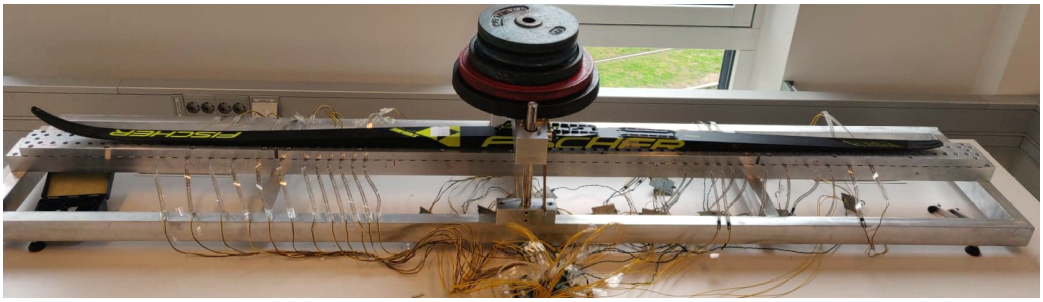

Figure 7.1: Measurement process for a cross-country ski, image illustrates one measurement cycle.

7.3.1 Pressure distribution

The first pressure distribution measurements conducted in the thesis was done to verify the output of the system. The measurements proved to show pressure data from the sensors; this was verified manually by physically checking the sensors for contact on the weight transfer pins. The first measurement for the 812 ski pair is shown in Figures 7.2 and 7.3 presented a summed

weight of 43.6470kg and 42.7202kg, and the 902 ski pair is shown in Figures 7.4 and 7.5 presented a summed weight of 46.2460kg and 43.3244kg. The sum of measured weights show a significant deviation from the actual loaded weight. This is further discussed in Section 8.1. The figures show each channel on the mechanical system separately, each channel together and then the average of both channels. Both skis from the 812 ski pair from Figures 7.2 and 7.3, show a significant similarity in load values on channel 1. The two peaks in the front side of the ski are lower than the dominant peak on the back section of the ski. The average channel for both skis in the 812 ski pair show similar trends were the front area has lower pressure and an extended contact area in the front, and a small contact area with a steep pressure curve on the back of the ski. When comparing the 902 with the 812 ski pair, the 902 ski pair in Figures 7.4 and 7.5, has approximately two equally loaded pressure areas in the front and back, with some tendencies of a steeper increase of pressure closer to the camber pocket. On the outer side of the pressure areas, the pressure is slowly converging towards no contact. The 902 ski pair also show an overall longer contact area for the front and back section of the ski compared to the 812 pair. Even though the pressure differs for each ski in both ski pairs, the tendencies in the pressure distributions are similar.

7.3.2 Repeatability and Accuracy

Following the initial measurements, each ski was tested ten times as described in Section 7.3. These measurements had the aim of verifying the consistency in the results for every measurement. It was essential to investigate whether results from the same ski were similar over several attempts. The standard deviation and mean value for all sensor indexes were calculated and presented as error plots. The error plot for the 812 ski pair is presented in Figures 7.6 and 7.7, and for the 902 ski pair in Figures 7.8 and 7.9. The load data presented in the figures show larger variations in most of the sensor indexes over the ten measurement cycles. The variation in each sensor index is related to the maximum deviation error calculated for each sensor and its system function. From Figure 7.6, a more significant variation can be seen at the sensors placed at 425 mm. This sensor location translates to sensor position 12 from the pressure distribution plot. By comparing the maximum deviation from linearity from sensor 12 (see Appendix 9.1, Table 6.4) with the variation in the error plot, we can see the source for the variation in the pressure distribution at sensors in the 12^{th} position.

The sum of all load data from the sensors for each measurement cycle is collected to verify that the mechanical system is registering the actual

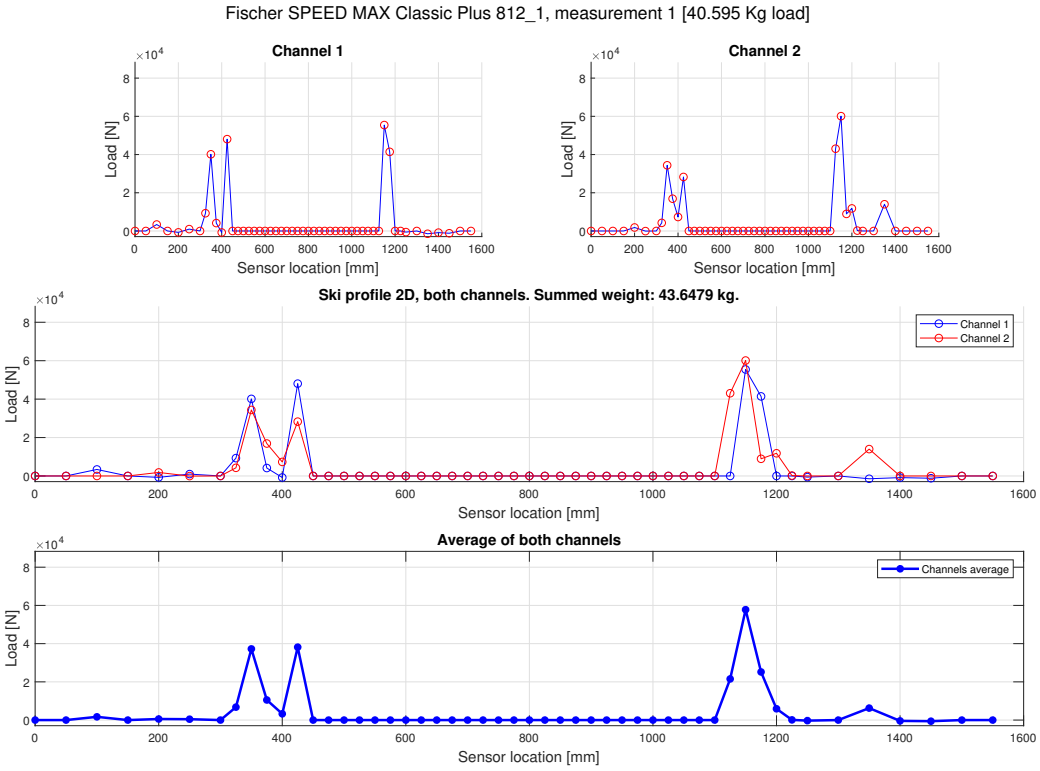

Figure 7.2: Pressure distribution plot for Speedmax Classical Plus 812_1, for measurement 1.

weight loaded (i.e., verifying repeatability). Figure 7.10 shows box plots of the summed weight for all 10 measurements for each ski. The variation in the measured weights is represented in standard deviation from the median value for the individual skis. The standard deviation and mean values are calculated and presented in Table 7.1. The measured ski that presents the highest standard deviation are the 812_1 and 902_1 skis seen in Figure 7.10 and Table 7.1. These two skis also have the lowest accuracy and slightly lower precision compared to the 812_2 and 902_2 skis. The measured ski with both the highest accuracy and precision is the 902_2 ski with an average weight sum of $43.97kg$ (see Section 8.1 for further discussion of the deviation from actual loaded weight).

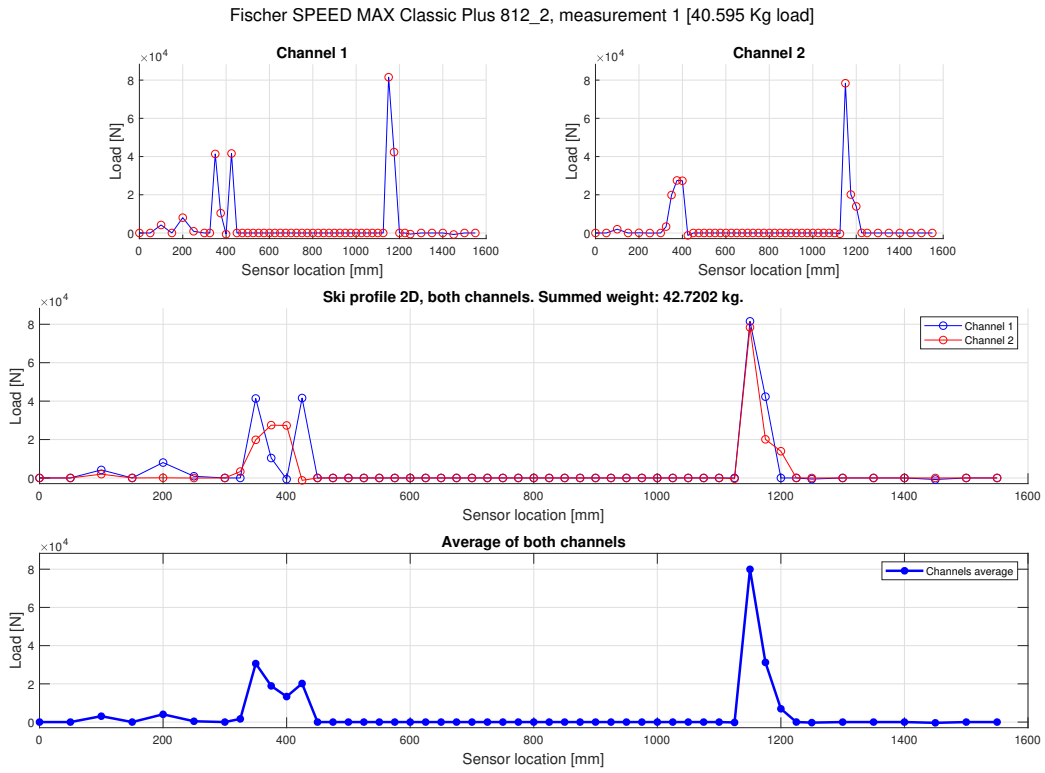

Figure 7.3: Pressure distribution plot for Speedmax Classical Plus 812_2, measurement 1.

7.4 Visualizing the pressure distribution

Heat maps have been generated to help visualize the pressure distribution. The amount of load on the surface from the ski is illustrated with colors; a brighter color represents higher pressure on the surface. The heat maps for the 812 ski pair is shown in Figures 7.11 and 7.12, and the 902 ski pair in Figures 7.13 and 7.14. The heat maps were generated by padding the two-dimensional pressure distribution array with zeros and applying an interpolating shading effect to extend the pressure areas in both dimensions. The heat maps consists of a 4 x 51 matrix were only the two middle rows in the matrix represent the actual measured values.

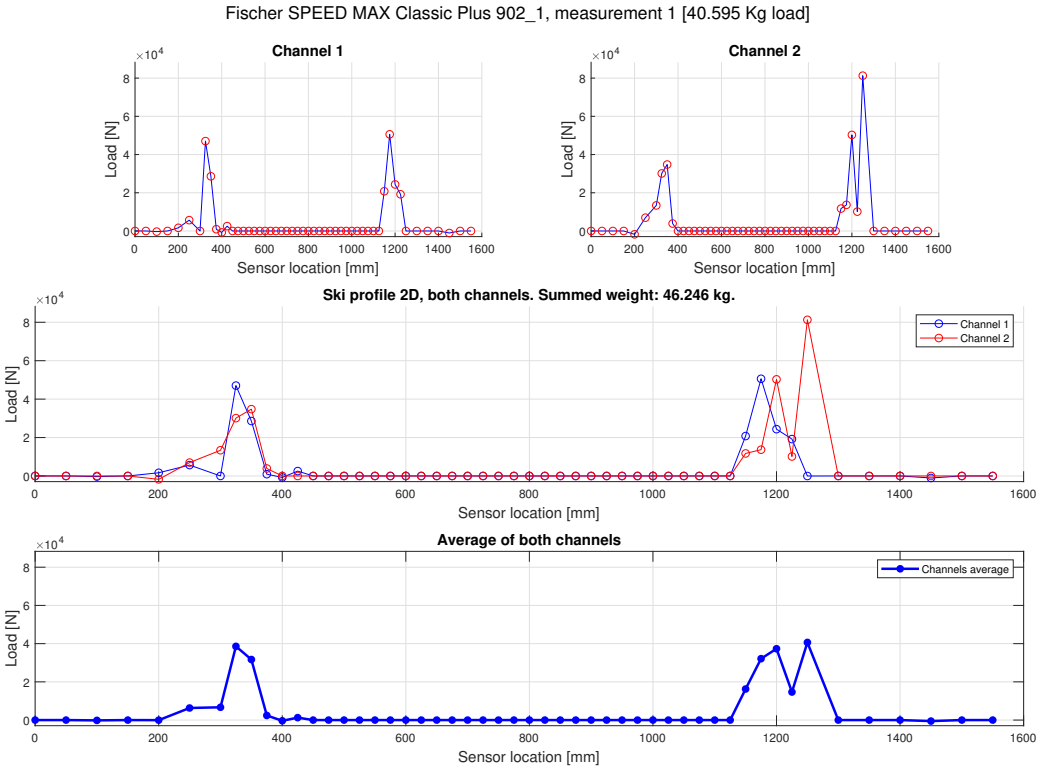

Figure 7.4: Pressure distribution plot for Speedmax Classical Plus 902_1, measurement 1.

7.5 Matching cross-country skis

One possible way of matching cross-country skis is by using a correlation method between two ski profiles like the ones shown in Figures 7.2 and 7.5. A correlation between ski profiles will tell us which two ski profiles are most similar. For this system, the quality of matching have two alternatives; the first option is to compare the average pressure distributions to find the skis with most similar pressure distribution, while the second option is to compare each channel of the ski profiles. The second options offer more specific pressure distribution matching to also account for twisting. The correlation coefficient from the correlation is a measure of the similarity between ski profiles, and with more ski measurements, this method could be a way of matching skis.

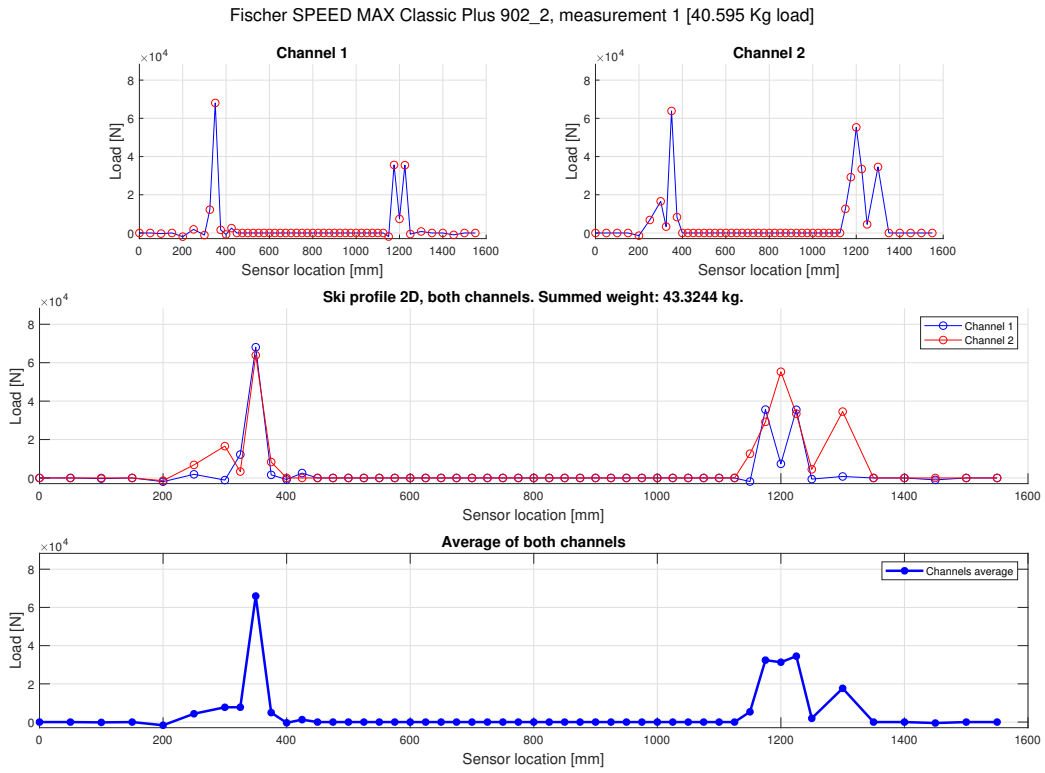

Figure 7.5: Pressure distribution plot for Speedmax Classical Plus 902_2, measurement 1.

7.6 Detecting warm and cold skis

By inspecting Figures 7.6 and 7.7, we can confirm that the *Speedmax Classic Plus 812* ski pair is more suitable for cold weather and snow conditions than the *Speedmax Classic Plus 902*. This can be understood from investigating the peaks on either side of the camber pocket. The back peaks are in general higher than the front peaks, while the front pressure zones have extended contact zones compared to the 902 ski pair in Figures 7.8 and 7.9. The extended pressure zone could correspond to the characteristics explained in Section 7.1. Investigation of the figures for the 902 ski pair shows higher pressure in the contact zone closer to the camber pocket. This causes the camber pocket to gain camber height closer to the contact zones slightly faster compared to the 812 ski pair. Due to the faster growth in camber height after the contact zone, a warm ski assumption can be made. This assumption

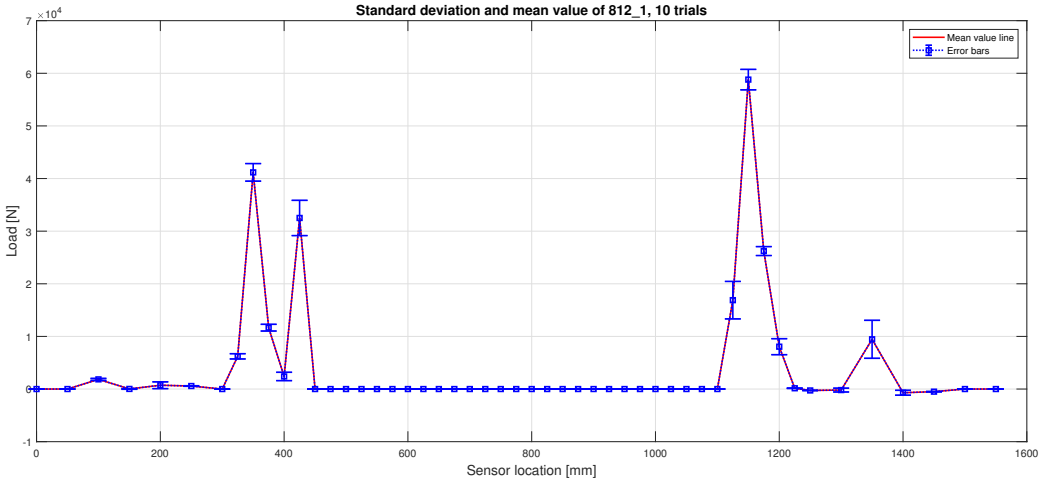

Figure 7.6: Pressure distribution error plot for Speedmax Classical Plus 812_1, standard deviation is presented as the end caps on each data point and a mean value line.

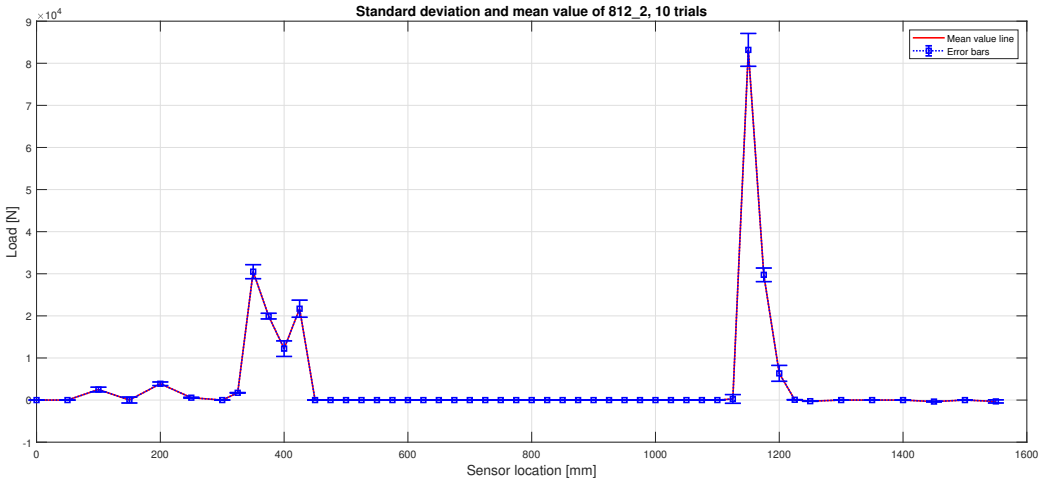

Figure 7.7: Pressure distribution error plot for Speedmax Classical Plus 812_2, standard deviation is presented as the end caps on each data point and a mean value line.

aligns with the description from Section 7.2. This will be discussed in detail in Section 8.2.

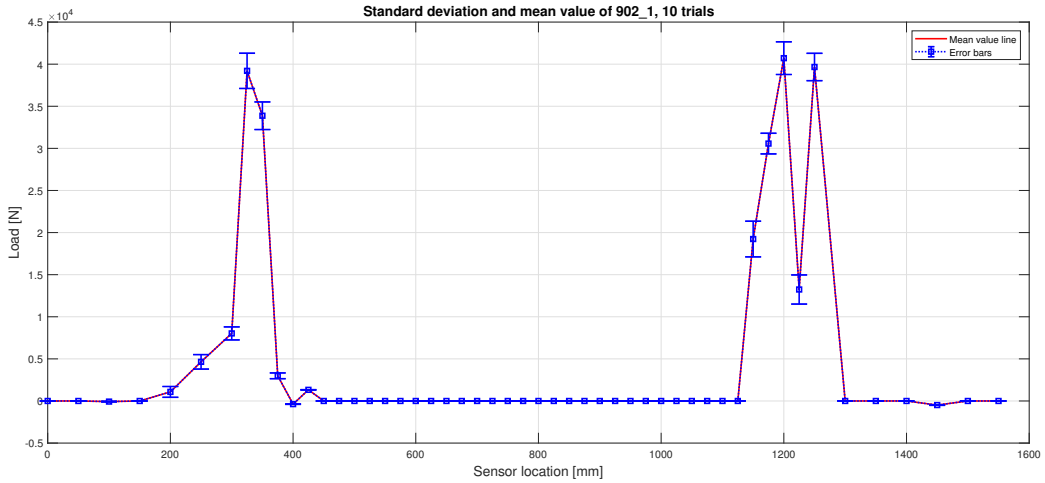

Figure 7.8: Pressure distribution error plot for Speedmax Classical Plus 902_1, standard deviation is presented as the end caps on each data point and a mean value line.

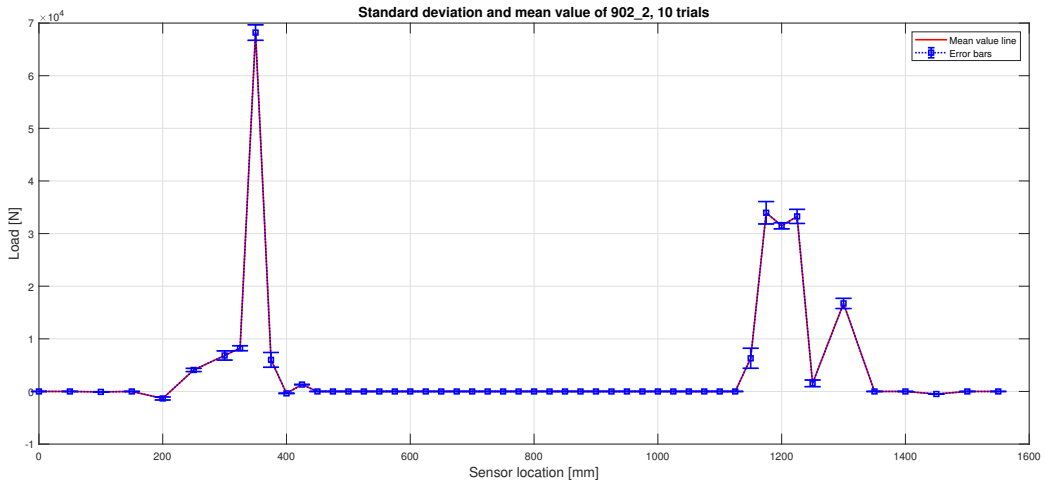

Figure 7.9: Pressure distribution error plot for Speedmax Classical Plus 902_2, standard deviation is presented as the end caps on each data point and a mean value line.

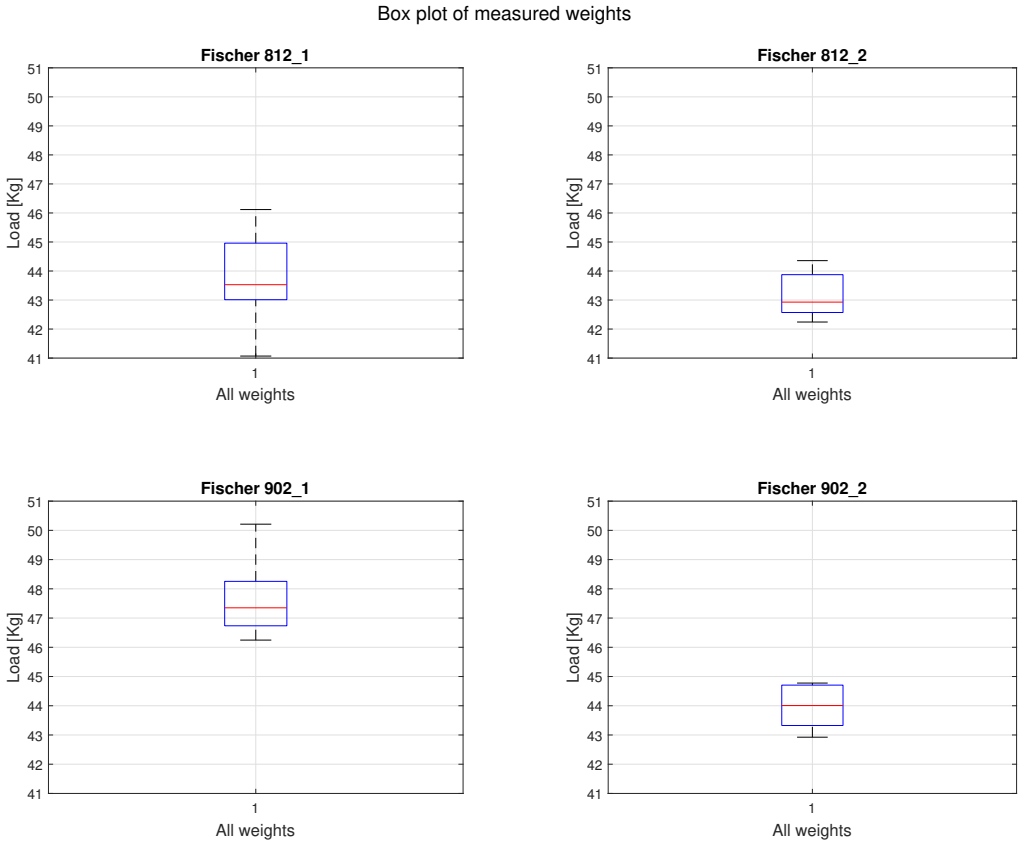

Figure 7.10: The plot shows the median value as the red lines and outliers on the top and bottom caps for ten trials on all skis.

Trial	**812_1** (Kg)	**812_2** (Kg)	**902_1** (Kg)	**902_2** (Kg)
1	43.648	42.720	46.246	43.324
2	44.960	42.490	47.242	43.620
3	42.632	43.137	46.544	42.924
4	45.463	44.357	46.736	43.807
5	46.117	43.874	47.916	44.776
6	41.069	44.144	48.602	44.710
7	44.898	43.524	47.459	44.208
8	43.409	42.617	47.112	44.706
9	43.011	42.242	50.212	44.638
10	43.121	42.571	48.255	42.992
Mean	43.833	43.168	47.632	43.971
σ	3.070	1.557	1.953	1.4692

Table 7.1: Sum of measured weights from each trial.

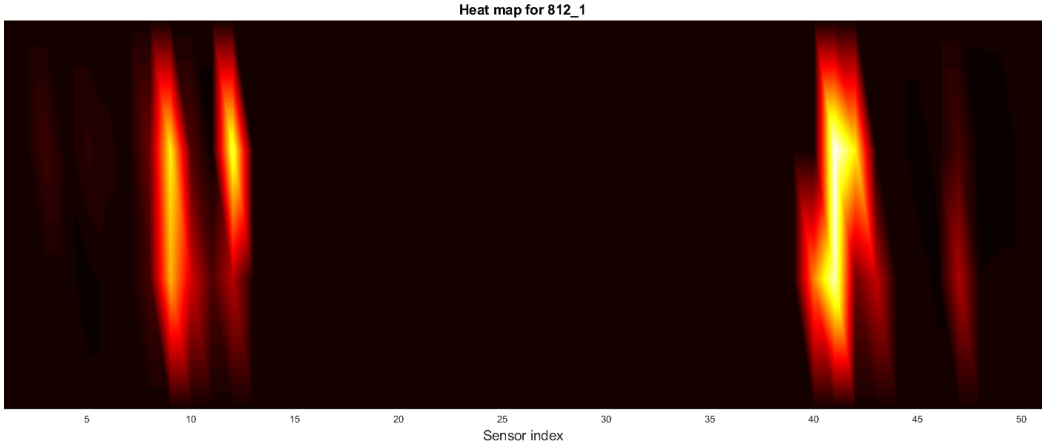

Figure 7.11: Heat map of pressure distribution for Speedmax Classical Plus 812_1, average of ten measurements.

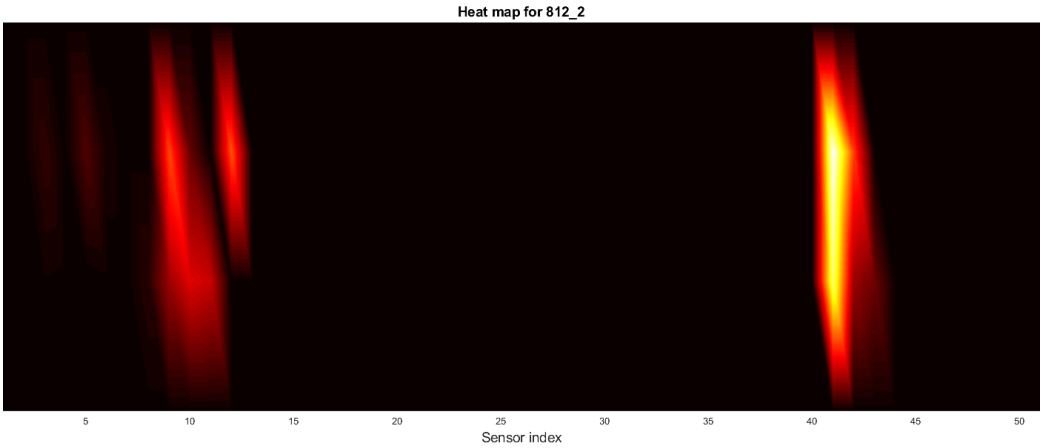

Figure 7.12: Heat map of pressure distribution for Speedmax Classical Plus 812_2, average of ten measurements.

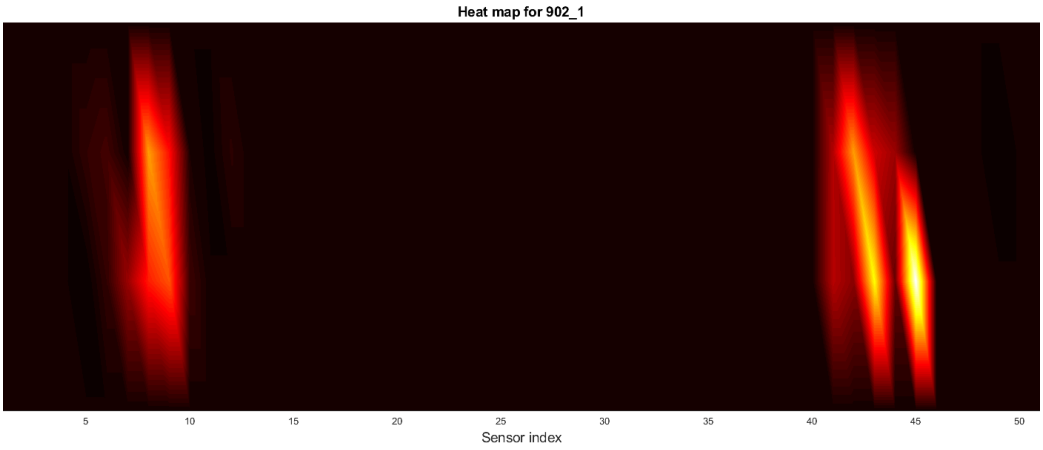

Figure 7.13: Heat map of pressure distribution for Speedmax Classical Plus 902_1, average of ten measurements.

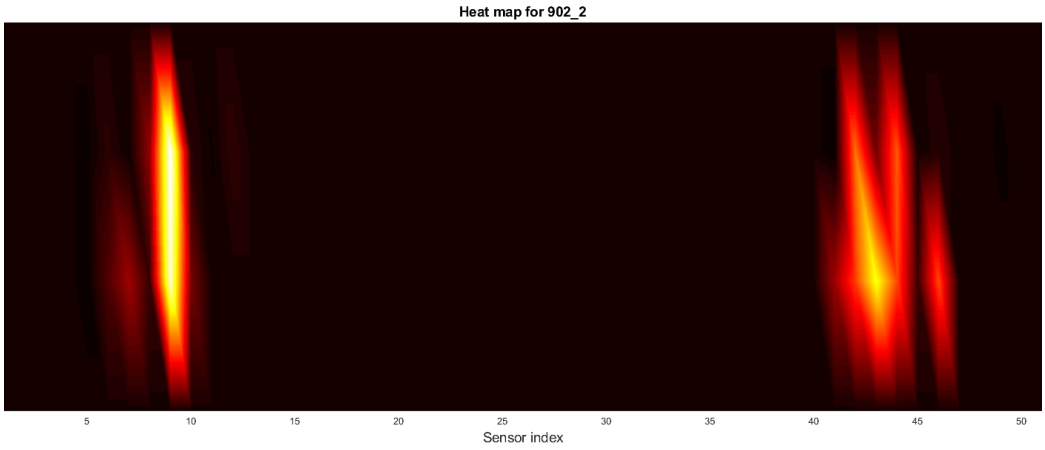

Figure 7.14: Heat map of pressure distribution for Speedmax Classical Plus 902_2, average of ten measurements.

Chapter 8

Discussion

Chapter abstract: *This chapter discusses the results presented in Chapter 7. Several aspects of the pressure distribution are considered, like how the characteristics of the pressure distribution can contribute to increased gliding speeds. While many of these theoretical aspects remain assumptions, they require practical testing for confirmation.*

8.1 Pressure distribution

The pressure distribution results presented in Section 7.3.1 show measurement errors that are significantly impacted by the calibration of some sensors. The evaluation of the accuracy was done by summing and comparing the total measured force from the sensors with the actual weight. Some of the skis had a higher difference in total measured weight from the actual loaded weight of $40.6kg$. This difference between the skis measured could be explained by referring to the system function for each sensor. The 812_1 ski which had the highest standard deviation of $3.07kg$ from the measured weights in Table 7.1, also had more contact with sensors at the 12^{th} position, which had a high calibration error. The two sensors at 12^{th} position ($425\ mm$) had a maximum deviation from linearity of 12.02 % and 18.25 % (see Table 9.1). The 902_2 ski had a significant load at 9^{th} sensor position and had the lowest deviation in total measured weights. The sensors at 9^{th} position had a maximum deviation from linearity of 5.67 % and 4.01 % (see Table 9.1) which explains the lower deviation in summed weights compared to the 902_2. The large deviation and low precision of the summed weight for all the skis can indicate that the system is not suited to conduct quantitative measurements with the current calibrations of the sensors. More accurate calibration of these sensors could result in lower standard deviation

in the measured weights and present better results in terms of repeatability and accuracy. It was desired to investigating each channel from a ski profile separately to look for twisting in the skis. By reading a higher value on one of the channels for the same sensor index could indicate twisting in the ski. In cases where the values on the same sensor index are the same, it may indicate that the pressure is distributed equally on both sides of the ski. A homogeneous contact area where the pressure is distributed equally on both sides can lead to even frictional melting, thus giving increased gliding speeds. The results presented in Section 7.3.1, showed repeatable results on channel 1 for almost every occasion, where channel 2 had more substantial variations for some sensors. Because of the variations in channel 2 compared to channel 1, investigating twisting in the ski was a challenge. On the other hand, if all the calibrations had a similar maximum deviation from linearity error and all sensors were equal, one could theoretically see tendencies of twisting in a cross-country ski by comparing the amount of load on each sensor index for both channels.

8.2 Detecting cold and warm ski profiles

The basic assumption on weather and snow conditions for a ski can be made by investigating the pressure distribution plots. A clear difference could be seen for the Fischer Speedmax Classic Plus 812 ski pair compared to the Fischer Speedmax Classic Plus 902 ski pair. Finding consistent tendencies on both ski profile types for several cross-country skis would be necessary to confirm the cold and warm ski assumptions. Rønbeck (2001) further explains the advantages of an extended pressure zone for cold weather and snow conditions, which may contribute to increased water film thickness. Tendencies of longer contact area can be seen for both skis in the 812 ski pair from Figures 7.6 and 7.7. The highest load is presented closer to the heel close to the camber pocket, while tendencies of contact in the front section at sensors 3 and 5 can be seen toward the tip of the ski. The contact at sensor 3 and 5 could confirm the extended contact characteristics of the ski provided by the ski manufacturer. The 812 ski pair has an overall steeper slope and a higher load represented on the back section compared to the front section of the ski. The extended front pressure zone could result in prolonged frictional melting over a more extended surface area, which may be required for cold weathers were water is absent. While considering cross-country skis for warm weather and snow conditions, increased pressure closer to the camber pocket in the 902 ski pair can be seen in Figures 7.8 and 7.9. This could verify the increased camber height in the transition from contact to camber pocket com-

pared to the 812 ski pair. Due to the absence of camber height measurements we cannot confirm if higher pressure close to the camber pocket is causing a steeper camber pocket. An assumption on cross-country skis for warm weather and snow conditions can be made with similar mechanical properties like the 902_1 ski, where the load is equally divided on both the front and back section of the ski, thus reducing the contact area. A shorter contact area may contribute to reducing the water film thickness where thicker water films may cause drag on the ski sole (Rønbeck 2001). The equal amount of load on both sections could also indicate a faster increase in camber height for both sides of the camber pocket.

8.3 Measurement quality

The measurement quality of the system was affected by multiple sources of variations and errors. These sources were first and foremost variations in each sensor, which made the calibration process challenging. Each sensor required a specific system function in an attempt to remove sensor variations affecting the overall measurement quality. In terms of the circuit variations, the only source of variation was the difference in the operating voltage range supplying the operational amplifier for each circuit. This difference in voltage range could be affecting the offset bias in each of the system function for the sensors, making the calibration errors higher. The overall size of the errors is multiplicative for each source of hardware presented to the system (i.e., fewer circuits with an increased number of sensor inputs per circuit could improve the measurement quality). Another source of error was presented in the sampling process in MATLAB®. While trying to sample all sensors for several sampling cycles, a cumulative increase in output voltage could be seen while measuring. We were not able to resolve this issue, due to time restrictions and lack of in-depth knowledge with the Arduino Uno Rev3. This source of error could have come from the multiplexer board (MUX Shield II) placed on top of the Arduino MCU. For each cycle of sampling, the input voltages could be cumulative increasing because of the capacitance in the ADC. Furthermore, sampling accuracy of the ADC in the Arduino Uno Rev3 was affected by the lack of software support in MATLAB®. The reference voltage was set to $5\ V$, whereas our operating voltage range capped at $3.98\ V$. The absence of $5\ V - 3.98\ V = 1.02\ V$ resulted in losing the sampling resolution in the top $1.02\ V$ of the ADC. If the reference voltages were adjustable through MATLAB®, the measurements could have been read more accurately by the ADC due to the resolution of $2^{10} = 1024$ being spread over $3.98\ V$ instead of $5\ V$. The last source of error found was in

the FlexiForce A201. The HIGH version (i.e., up to 445 N) proved to have a steep increase in resistance values for the higher range of weights[1] shown in Figure 5.5. A lower version of the A201 sensor, for example, MEDIUM (i.e., up to 111 N) could result in a more even and flatter slope in resistance values for weights encountered in the measurements. A lower slope in resistance could, in theory, allow the ADC to detect the lower part of the spectrum more accurately compared to the current setup.

8.4 Friction affected by mechanical properties

A homogeneous latitudinal pressure zone in the front section of the ski can be seen for the 902_2 ski in Figure 7.14. This pressure zone could indicate a good example for a cross-country ski for even frictional melting across the latitudinal length in the front section of the ski. The load represented at this location could be used to calculate the kinetic frictional forces working at this area. Due to the uncertainty of the represented load compared to the actual load on this location, an approximation of the kinetic frictional forces could be calculated.

8.5 How to choose a ski

Determining the choice of skis for different weather and snow conditions, we investigated the mechanical properties and how they relate to snow and weather and snow conditions. Choosing the ideal ski for the given snow condition can be based on the stiffness of the ski, as was done by Breitschädel (2014). For Classic skis, the choice of stiffness was around 66% and 67% of the body weight for men and women respectively and for warm conditions an increase to 77% for both men and women (Breitschädel 2012).

Adjusting factors such as gliding wax and mechanical properties of the ski for different weather and snow conditions and temperatures can result in better gliding speeds (Breitschädel 2012). In addition to these adjustable factors, a cold and warm condition was defined for each pair of skis. The skis for warm conditions are typically stiffer. The aspect of pairing two skis with equal characteristics have been considered earlier. As an example, Bäckström, Dahlen, and Tinnsten (2008) published a paper describing a ski

[1] Due to the resolution of the ADC, smaller changes in resistance values are more detectable in the higher range of weights.

measurement system the Swedish cross-country team in 2008 had been using for 2.5 years to match mechanical properties in skis. This resulted in faster and more accurate matching of cross-country skis.

Chapter 9

Conclusion

The process of collecting pressure distribution data from cross-country skis includes many steps, where each element contributes to the quality of the values extracted. From finding a proper sensor that characterizes as linear and the circuits that produce stable voltage outputs, to the quality of the analog-to-digital converters for sampling. The main objective of the thesis was to find a way to produce this pressure distribution data with commercially available pressure-sensitive film sensors like the FlexiForce A201 sensor. Chapters included in this thesis have all helped to make objective choices for the further development of the system. This process has been long and informative. The most comprehensive chapter was Chapter 5, where circuit electronics is a broad and comprehensive field. It was preferred to investigate more cross-country skis in-depth in this thesis in order to achieve more tangible data.

By developing a mechanical system presented in this thesis, cheaper commercially available pressure-sensitive film sensors can be used to measure the pressure distribution of skis with the help of; accurate arranged placement of the sensors along the longitudinal length of the ski with underlying *pucks*, designed circuits with low noise outputs and a microcontroller unit to sample the voltage data (**A**). The mechanical system can recognize the difference in each cross-country ski measured. Assumptions can be made on either if the ski is best suited for cold or warm weather and snow conditions. Due to the lack of pressure distribution data and uncertainties in the measurements discussed in Section 8.1, we can not say for sure the suited weather and snow conditions for skis. The measured results were also affected by the resolution of the ADC in the Arduino Uno Rev3. Reference voltage used by the ADC is commonly adjustable to change the operation range of the ADC. While using the *MATLAB Support Package for Arduino Hardware* in MATLAB®, the reference voltage was not supported for adjustment. We ended up losing

$\frac{1}{5}$ of the ADC resolution, which caused additional effects on the measurement quality.
With the current state of the system producing different results for each measurement cycle for all four skis, it cannot produce reliable results. Even though the system can detect the difference in each ski, the variations and the standard deviation in the measurements is too fluctuating to draw a solid conclusion on ski quality and to investigate twisting in cross-country skis (**B**). A new round of calibration is necessary to overcome the current calibration error in many of the sensors. Both the resting time between each weight interval and the loading time of the sensors during calibration was accounted for, but a more methodical process during calibration is necessary.

The amount of static and kinetic frictional forces between the ski sole and the surface can be calculated for different sole materials, but with the same error in the calculations as a combined error from the measurement system. On the last note, we were not able to investigate pressure distribution characteristics with loads offset from the binding point, due to the faulty design of the mechanical foot on the linear weight guide.

9.1 Further work

The measurement device needs further work and improvements to operate with acceptable errors below ± 3 %. The FlexiForce A201 HIGH sensor used in this master project was better suited for weights in the higher spectrum closer to a skiers FBW. The investigation with HBW weights led to speculations on using a different sensor. The FlexiForce A201 MEDIUM would be more suited in our case, where the maximum weight limit of the sensor is 111 N. By implementing this version of the A201 sensor, the $R_{feedback}$ resistor would also need to be adjusted for all the circuits. We believe that the circuit characteristics would be overall flatter and more sensitive to changes in weight from 0 kg to 10 kg. Furthermore, the MCU could be upgraded. One ADC proved challenging to operate on 48 inputs. An MCU with more than one ADC and a faster CPU would improve the operating speed of the system in terms of sampling. Additional sensors can be implemented to increase the resolution of the contact zones on the surface, thus allowing for a better understanding of the pressure distribution. The malfunctioning adjustable foot could be redesigned to allow for the investigation of weight offsets from the binding point. The adjustable foot could also introduce more even load transfer from the linear weight guide to the ski binding.

Bibliography

Analog Devices, Inc. 2009. "Sample-and-Hold Amplifiers". https://www.analog.com/media/cn/training-seminars/tutorials/MT-090.pdf.

Arduino AG. 2019. "Arduino Uno Rev3". Visited on 07/14/2019. https://store.arduino.cc/arduino-uno-rev3.

Bäurle, L, D Szabó, M Fauve, H Rhyner, and ND Spencer. 2006. "Sliding friction of polyethylene on ice: tribometer measurements". *Tribology Letters* 24 (1): 77–84.

Bowden, FP. 1953. "Friction on snow and ice". *Proceedings of the Royal Society of London. Series A, Mathematical and Physical Sciences* 217 (1131): 462–478.

Bowden, FP, and TP Hughes. 1939. "The mechanism of sliding on ice and snow". *Proc. R. Soc. Lond. A* 172 (949): 280–298.

Breitschädel, Felix. 2014. "Technical aspects to improve performance in cross-country skiing". Visited on 05/03/2018. https://brage.bibsys.no/xmlui/handle/11250/232880.

— . 2012. "Variation of Nordic Classic Ski Characteristics from Norwegian national team athletes". *Procedia Engineering*, ENGINEERING OF SPORT CONFERENCE 2012, 34:391–396. ISSN: 1877-7058, visited on 05/03/2018. doi:10.1016/j.proeng.2012.04.067. http://www.sciencedirect.com/science/article/pii/S1877705812016803.

Bäckström, M., L. Dahlen, and M. Tinnsten. 2008. "Essential Ski Characteristics for Cross-Country Skis Performance (P251)". *The Engineering of Sport 7*: 543–549. Visited on 05/03/2018. doi:10.1007/978-2-287-09413-2_66. https://link.springer.com/chapter/10.1007/978-2-287-09413-2_66.

Colbeck, S.C. 1986. "Classification of seasonal snow cover crystals". *Water Resources Research* 22 (9 S): 59S–70. ISSN: 00431397.

Day, Robert A. 2011. *How to write and publish a scientific paper*. Santa Barbara, Calif.

Erkkilä, J. 1986. *Studies of the mechanical properties of cross-country skis*. Finnish Academy of Technical Sciences.

FIS cross-country. 2018. "Cross-country results". Visited on 07/05/2018. http://www.fis-ski.com/.

Fraden, Jacob. 2005. *Handbook of Modern Sensors: Physics, Designs, and Applications*. Fifth edition. New York City: Springer.

Fritsch GmbH. 2019. "Manual pick & place device". Visited on 07/14/2019. https://www.fritsch-smt.de/en/manual-pick-place/lm900/.

Gear West. 2011. "Gear West Signature Flex Tester". Visited on 07/29/2019. http://gearwestxcskiing.blogspot.com/2011/06/gear-west-ski-flex-tester.html.

— . 2018. "SkiDNA measurement device". Visited on 07/29/2018. https://gearwest.com/skiDNA.

He, F. 2015. "USB Port and power delivery: An overview of USB port interoperabiliy", 1–5. 2015 IEEE Symposium on Product Compliance Engineering (ISPCE).

Hollinger, Avrum, and Marcelo M. Wanderley. 2006. "Evaluation of commercial force-sensing resistors". In *Proceedings of the International Conference on New Interfaces for Musical Expression, Paris, France*, 4–8.

IDT Sport. 2018. "IDT Sport measurement device". Visited on 07/29/2018. https://www.idt.no/sport/produkter/skianalyzer/skianalyzer.

Interlink Electronics. 2019. "Interlink Electronics 402 Short". Visited on 01/25/2019. https://www.interlinkelectronics.com/fsr-402-short.

MathWorks. 2019. "MATLAB® environment". Visited on 07/15/2019. https://se.mathworks.com/products/matlab.html.

Mayhew Labs. 2019. "MUX Shield II". Visited on 07/14/2019. http://mayhewlabs.com/products/mux-shield-2.

Milsluker'n. 2019. "Fischer Speedmax Classic Plus IFP (18/19 mod)". Visited on 07/26/2019. https://www.milslukern.no/product.html/fischer-speedmax-classic-plus-ifp-17/18-mod.

Nilsson, Johnny, Lars Karlöf, and Vidar Jakobsen. 2013. "A new device for measuring ski running surface force and pressure profiles". *Sports Engineering* (London) 16 (1): 55–59. ISSN: 1369-7072.

Oslo Sportslager. 2019. "Fischer SpeedMax Classic Plus 902 (18/19 mod)". Visited on 07/26/2019. https://www.oslosportslager.no/produkt/fischer-rcs-speedmax-classic-plus-902-langrennski-1819-45114.aspx.

Paden, Frederick T. 1954. "Early test bench" (): 3. Visited on 07/01/2018. https://patents.google.com/patent/US2693107A/.

Pallas-Areny, Ramon, and John G Webster. 2001. *Sensors and signal conditioning*. Second edition. John Wiley & Sons.

Rubicson. 2019. "Rubicson Digital Kitchen weight". Visited on 07/29/2019. https://www.kjell.com/no/produkter/elektro-og-verktoy/verktoy/maleinstrumenter/vekter/kjokkenvekter/rubicson-digital-kjokkenvekt-svart-p48481.

Rønbeck, N. F. 2001. "Langrennski og snø". HiF-Rapport 2001:10.

Rønbeck, N. F, and N. O. Vikander. 2007. "Cross country ski technology: performance success-factors and barriers in an athlete for fair play perspective". (Vuokatti Sports Institut, Finland), Science and Nordic Skiing, Meyer and Meyer Series.

Ski-Test. 2018. "Eiker ski measurement device". Visited on 05/31/2018. http://www.ski-test.no/instructions/.

SkiSelector. 2018. "SkiSelector measurement device". Visited on 05/31/2018. http://www.skiselector.com/en/.

Tekscan, Inc. 2019. "FlexiForce A201 Standard Force & Load Sensors". Visited on 01/25/2019. https://www.tekscan.com/products-solutions/force-sensors/a201.

Vecchi, Fabrizio, Cinzia Freschi, Silvestro Micera, Angelo M. Sabatini, Paolo Dario, and Rinaldo Sacchetti. 2000. "Experimental evaluation of two commercial force sensors for applications in biomechanics and motor control".

Appendices

Circuit design

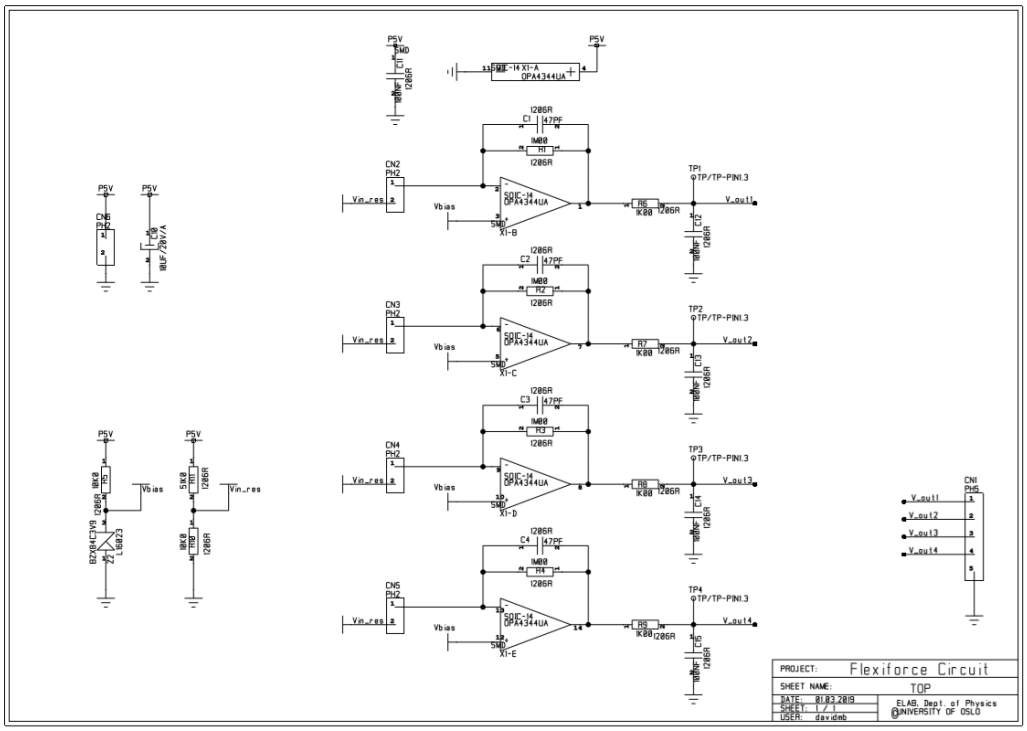

Figure 1: Design for biased inverting operational amplifier circuit.

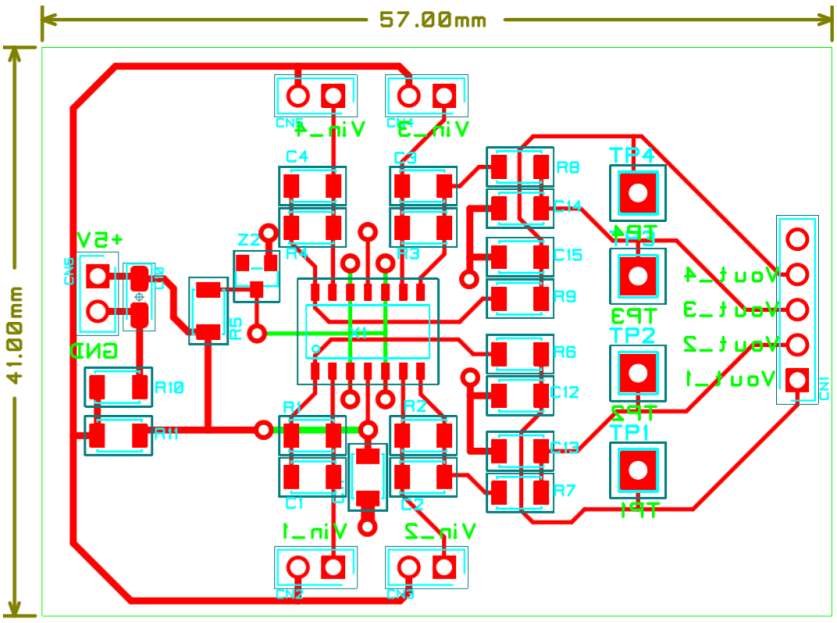

Figure 2: Etching map for biased inverting operational amplifier circuit.

Calibration values

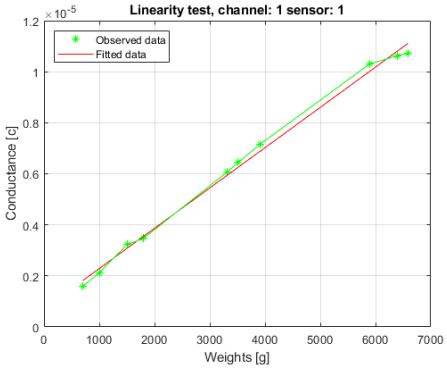

Figure 3: Linearity test of calibration; channel 1, sensor 1.

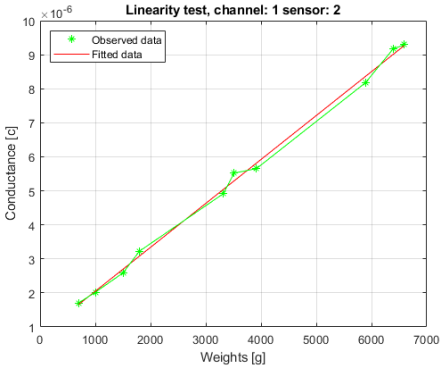

Figure 4: Linearity test of calibration; channel 1, sensor 2.

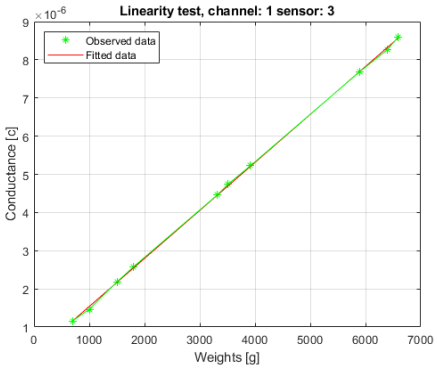

Figure 5: Linearity test of calibration; channel 1, sensor 3.

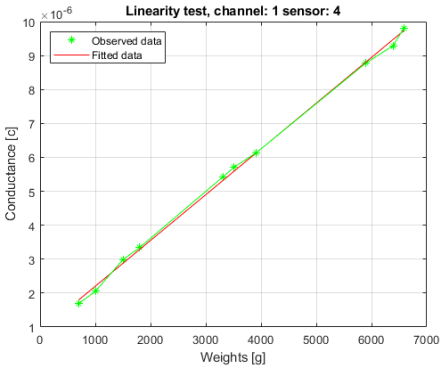

Figure 6: Linearity test of calibration; channel 1, sensor 4.

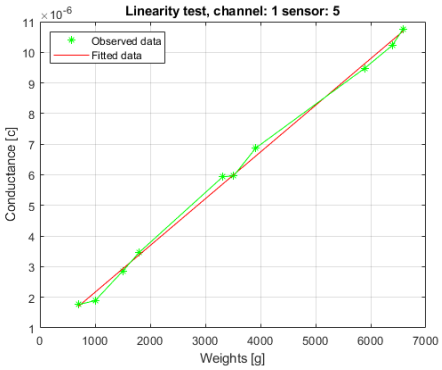

Figure 7: Linearity test of calibration; channel 1, sensor 5.

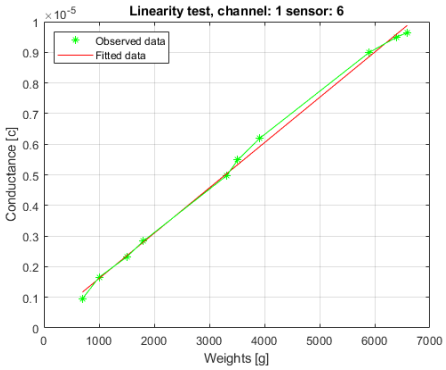

Figure 8: Linearity test of calibration; channel 1, sensor 6.

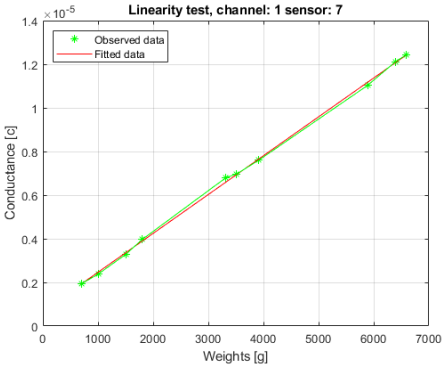

Figure 9: Linearity test of calibration; channel 1, sensor 7.

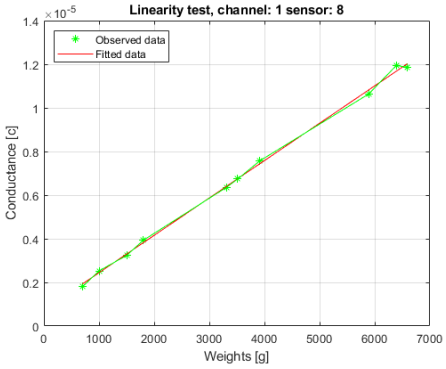

Figure 10: Linearity test of calibration; channel 1, sensor 8.

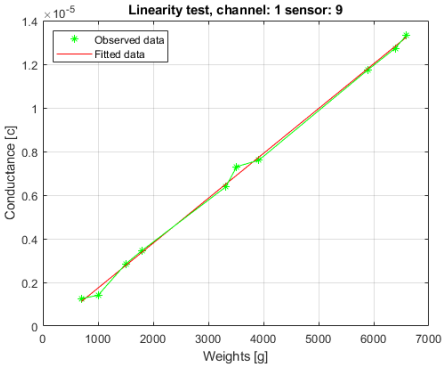

Figure 11: Linearity test of calibration; channel 1, sensor 9.

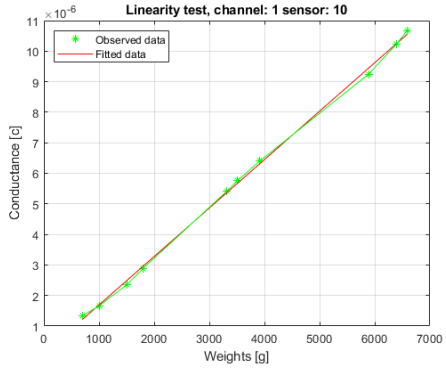

Figure 12: Linearity test of calibration; channel 1, sensor 10.

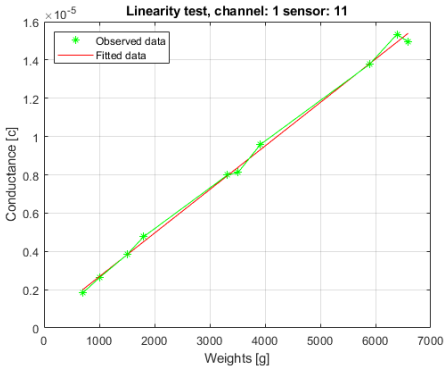

Figure 13: Linearity test of calibration; channel 1, sensor 11.

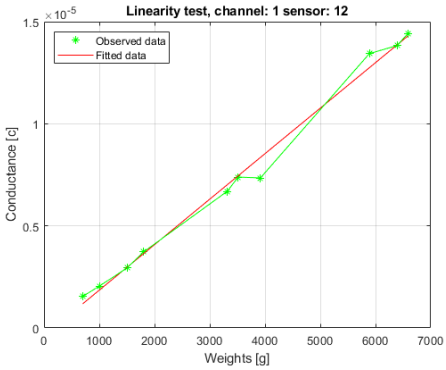

Figure 14: Linearity test of calibration; channel 1, sensor 12.

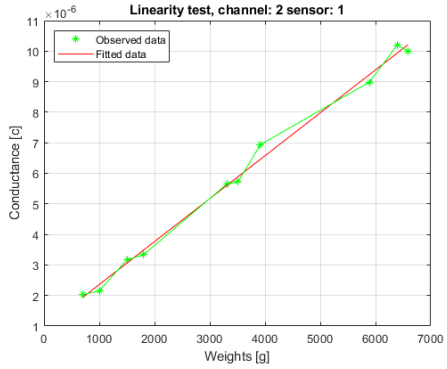

Figure 15: Linearity test of calibration; channel 2, sensor 1.

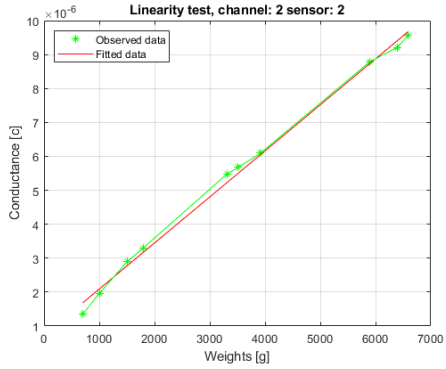

Figure 16: Linearity test of calibration; channel 2, sensor 2.

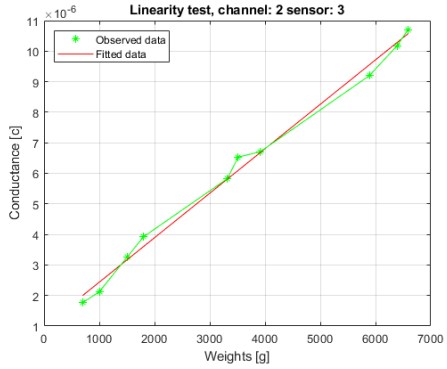

Figure 17: Linearity test of calibration; channel 2, sensor 3.

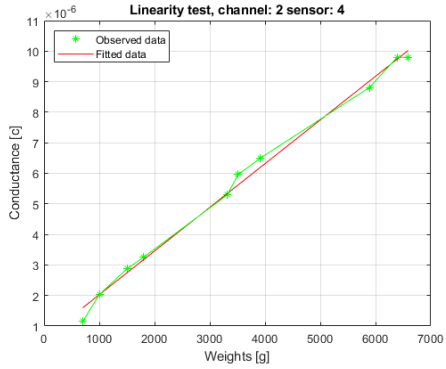

Figure 18: Linearity test of calibration; channel 2, sensor 4.

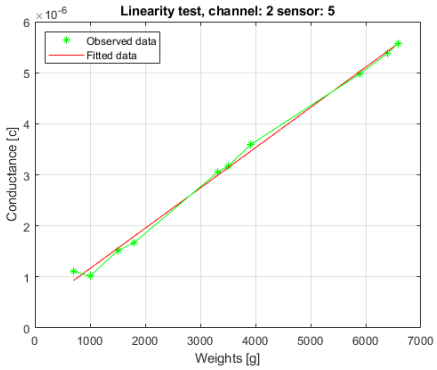

Figure 19: Linearity test of calibration; channel 2, sensor 5.

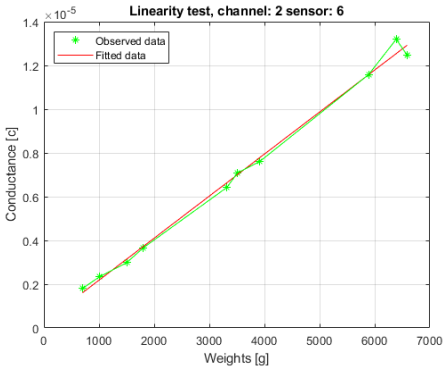

Figure 20: Linearity test of calibration; channel 2, sensor 6.

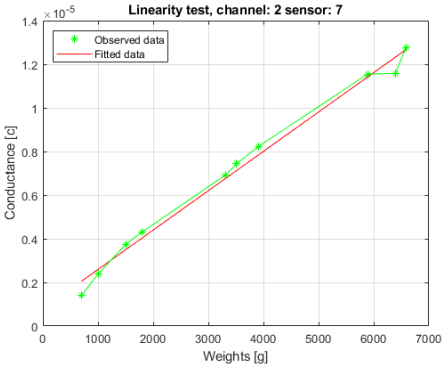

Figure 21: Linearity test of calibration; channel 2, sensor 7.

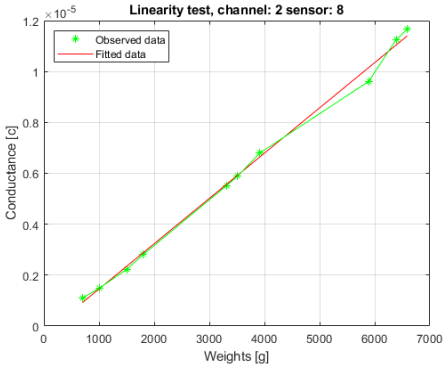

Figure 22: Linearity test of calibration; channel 2, sensor 8.

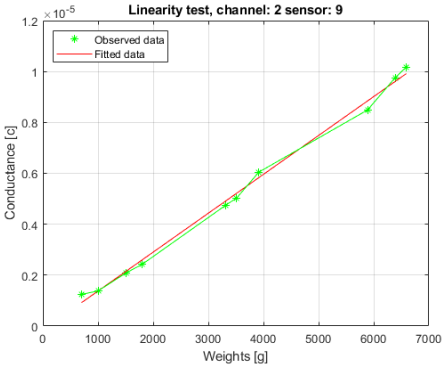

Figure 23: Linearity test of calibration; channel 2, sensor 9.

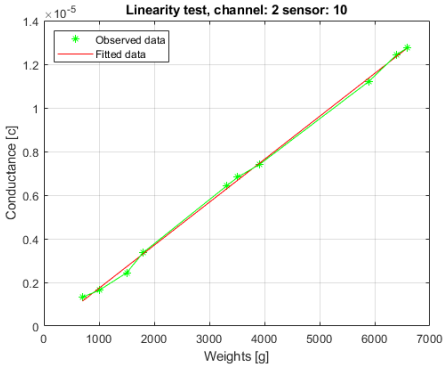

Figure 24: Linearity test of calibration; channel 2, sensor 10.

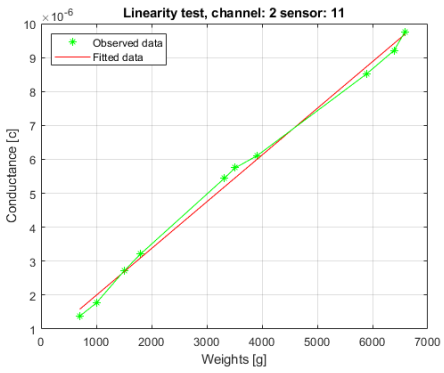

Figure 25: Linearity test of calibration; channel 2, sensor 11.

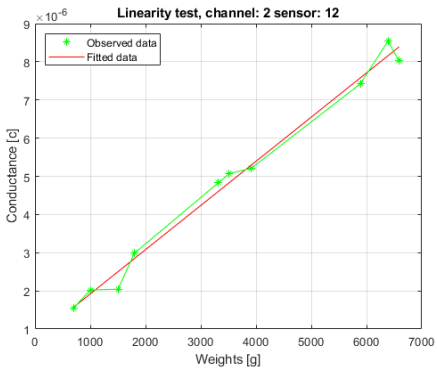

Figure 26: Linearity test of calibration; channel 2, sensor 12.

Channel	**Sensor**	**Maximum Deviation (%)**	**Maximum Deviation**
1	*1*	3.4619	$3.8464 \cdot 10^{-7}$
1	*2*	4.2950	$2.2744 \cdot 10^{-7}$
1	*3*	4.8202	$7.4252 \cdot 10^{-8}$
1	*4*	1.9057	$1.8048 \cdot 10^{-7}$
1	*5*	12.8473	$2.7818 \cdot 10^{-7}$
1	*6*	4.5551	$2.6990 \cdot 10^{-7}$
1	*7*	3.0705	$2.0233 \cdot 10^{-7}$
1	*8*	2.2427	$2.6186 \cdot 10^{-7}$
1	*9*	5.6674	$3.9185 \cdot 10^{-7}$
1	*10*	2.0893	$1.9732 \cdot 10^{-7}$
1	*11*	2.9214	$4.4959 \cdot 10^{-7}$
1	*12*	12.0216	$1.0038 \cdot 10^{-6}$
2	*1*	7.4169	$4.7902 \cdot 10^{-7}$
2	*2*	19.9530	$3.3621 \cdot 10^{-7}$
2	*3*	7.1079	$4.3342 \cdot 10^{-7}$
2	*4*	27.8801	$4.4551 \cdot 10^{-7}$
2	*5*	19.4898	$1.8085 \cdot 10^{-7}$
2	*6*	5.2083	$6.5310 \cdot 10^{-7}$
2	*7*	5.9676	$7.3503 \cdot 10^{-7}$
2	*8*	5.3405	$5.4219 \cdot 10^{-7}$
2	*9*	4.0102	$3.5472 \cdot 10^{-7}$
2	*10*	10.2433	$2.7871 \cdot 10^{-7}$
2	*11*	5.3443	$2.9168 \cdot 10^{-7}$
2	*12*	18.2454	$4.5659 \cdot 10^{-7}$

Table 1: Maximum Deviation from linearity calculations in terms of conductivity versus force. From calibrations of all FlexiForce A201 sensors in the mechanical system.

Matlab codes

.1 MUXanalogread.m

```
function [mux0array, mux1array, mux2array] =
    MUXanalogread(a)
    % MUX configuration, ref: Mayhew Labs User Guide
    % Reads voltage values from arduino link "a"
    % Selection pins used for selection
    S0 = 'D2';
    S1 = 'D4';
    S2 = 'D6';
    S3 = 'D7';
    % Arrays for storing voltage values
    mux0array = zeros(1,16);
    mux1array = zeros(1,16);
    mux2array = zeros(1,16);
    N = 4;
    temp = zeros(3,N);
    for i = 1:length(mux0array)
        j = i-1;
        a.writeDigitalPin(S0,bitand(j,1));
        a.writeDigitalPin(S1,bitshift(bitand(j,3),-1));
        a.writeDigitalPin(S2,bitshift(bitand(j,7),-2));
        a.writeDigitalPin(S3,bitshift(bitand(j,15),-3))
            ;
        % Choose 3 values for mean after 3 samples
        for j = 1:N
            temp(1,j) = a.readVoltage('A0');
            temp(2,j) = a.readVoltage('A1');
            temp(3,j) = a.readVoltage('A2');
        end
```

```
27          % Subtract 2% voltage error from the adc
28          mux0array(i)=mean(temp(1,1:end))-0.02*mean(temp
                (1,1:end));
29          mux1array(i)=mean(temp(2,1:end))-0.02*mean(temp
                (2,1:end));
30          mux2array(i)=mean(temp(3,1:end))-0.02*mean(temp
                (3,1:end));
31      end
32  end
```

.2 createSysFunc.m

```
1   function [r, sysfunc] = createSysFunc(a, weights, Vref,
        channel, sensor)
2       % Scripts for creating system function for a
            specific sensor
3       % with given weights and resistance values
4       r = zeros(1,length(weights));
5       Vout = zeros(1,3);
6       % For each weights, read voltage, calculate
            resistance value
7       for i = 1:length(r)
8           s = strcat('Load weight of: ', num2str(weights(
                i)), 'grams and press a key');
9           disp(s)
10          % wait for user input
11          pause;
12          for j = 1:length(Vout)
13              profile = createProfile(a);
14              Vout(j) = profile(channel, sensor);
15          end
16          % Calculate the resistance value for given
                voltage
17          r(i) = calculateResistance(mean(Vout), Vref(
                channel, sensor));
18      end
19      % Create the equation with polyfit
20      sysfunc = polyfit(weights, 1./r, 1);
21  end
```

.3 createProfile.m

```
function profile = createProfile(a)
    [io1, io2, io3] = MUXanalogread(a);
    io1_L = io1(1:2:end);
    io1_R = io1(2:2:end);
    io2_L = io2(1:2:end);
    io2_R = io2(2:2:end);
    io3_L = io3(1:2:end);
    io3_R = io3(2:2:end);
    profile = [io1_L, io2_L, io3_L; io1_R, io2_R, io3_R
        ];
end
```

.4 ArduinoSetup.m

```
function a = ArduinoSetup(com, type)
    % Establish arduino connection
    a = arduino(com, type,'Libraries','Adafruit\
        MotorShieldV2');
    shield = addon(a,'Adafruit\MotorShieldV2');

    % Selection pins used for selection
    S0 = 'D2';
    S1 = 'D4';
    S2 = 'D6';
    S3 = 'D7';

    % Set pinmodes for I/O's to OUTPUT mode, used for
        MUX Shield II
    a.configurePin(S0,'DigitalOutput');
    a.configurePin(S1,'DigitalOutput');
    a.configurePin(S2,'DigitalOutput');
    a.configurePin(S3,'DigitalOutput');
end
```

.5 calculateResistance.m

```
function r = calculateResistance(Vout, Vref)
    Rfb = 180*1e3;
    Vin = 4.839;
    %Vref = 3.874;
    r = Rfb * (Vin - Vref) / (Vref - Vout);
end
```

.6 main.m

```
%Version 3.0 - 01.07.2019
%@Petter Andre Kristiansen
%Main function for operating the measurement process
%Args:
%Functions:
%ArduinoSetup - Connection to arduino and MUX setup
%MUXanalogRead - Collects values from MUX shield II
%createSysFunc - Transfunc for each sensor
%createProfile - Voltage profile from all sensors
%calculateResistance - Calculates the resistance value
%% Setting up the arduino
arduino = ArduinoSetup('com3','uno');
%% Load workspace variables
load('data/27.06_measurement_workspace.mat')
%% Initialize variables
weight = @(gram) 0.5072*gram + 900;
weights2 = [700, 100 + weight(0), 500 + weight(200),
    900 + weight(0) ,...
    weight(4761), 200 + weight(4761), 500 + weight
        (4761+200), weight(5074.9+4761) ,...
    500 + weight(5074.9+4761), 700 + weight
        (5074.9+4761)];
plot(weights2); hold on; plot(weights2,'o');
title('Weight intervals for calibration')
xlabel('Interval #');
ylabel('Weight [g]');
% Vref = [circuit1, circuit2, ... , circuit12];
Vref = [ones(2,2)*3.847, ones(2,2)*3.837, ones(2,2)
    *3.864, ones(2,2)*3.857, ...
```

```
26      ones(2,2)*3.856, ones(2,2)*3.849, ones(2,2)*3.88,
           ones(2,2)*3.831, ...
27      ones(2,2)*3.86, ones(2,2)*3.856, ones(2,2)*3.876,
           ones(2,2)*3.841];
28  Vref_actual = createProfile(arduino);
29  % Sensor locations for plotting
30  hull_pitch = 25;
31  full_array_distance = [0:62]*hull_pitch;
32  I_array = logical([1 0 1 0 1 0 1 0 1 0 1 0 1 1 1 1 1 1
       0 0 0 0 0 0 0 0 0 0 0 0 0 0 ...
33      0 0 0 0 0 0 0 0 0 0 0 0 0 0 0 1 1 1 1 1 1 0 1 0 1 0 1
           0 1 0 1 0 1]);
34  x_axis_sensor_location = full_array_distance(I_array);
35  %% Setup data saving
36  ski_data_0107 = cell(4,3);
37  ski_data_fischer812_1 = cell(5,10);
38  ski_data_fischer812_2 = cell(5,10);
39  ski_data_fischer902_1 = cell(5,10);
40  ski_data_fischer902_2 = cell(5,10);
41  for i = 1:4
42      ski_data_0107{i,1} = x_axis_sensor_location;
43      ski_data_0107{i,2} = datetime('today');
44  end
45  %% Ten measurement cycles
46  skis = ["812_1", "812_2", "902_1", "902_2"];
47  for measurement = 1:10
48      clc;
49      disp(["Round: ", num2str(measurement)])
50      for ski = 1:4
51          s = skis(ski);
52          disp(s)
53          pause;
54          N = 2;
55          w_left = zeros(N,24);
56          w_right = zeros(N,24);
57          v = zeros(N,24);
58          r = zeros(N,24);
59
60          for sample = 1:N
61              v = createProfile(arduino);
62              r = arrayfun(@calculateResistance, v,
```

```
                Vref_actual);
63              for i = 1:length(w_left)
64                  w_left(sample,i) =  ((1./r(1, i) -
                        sysfunc_all{1,i}(2))./sysfunc_all{1,
                        i}(1));
65                  w_right(sample,i) = ((1./r(2, i) -
                        sysfunc_all{2,i}(2))./sysfunc_all{2,
                        i}(1));
66              end
67          end
68
69          w_left_avg = mean(w_left, 1);
70          w_right_avg = mean(w_right, 1);
71          w_left_avg(w_left_avg<-200) = 0;
72          w_right_avg(w_right_avg<-200) = 0;
73          w_profile = [w_right_avg;w_left_avg];
74          w_profile_avg = mean(w_profile,1);
75          w_total = (sum(w_left_avg) + sum(w_right_avg))
                /1000;
76
77          if ski == 1
78              ski_data_fischer812_1{1,measurement} =
                    w_profile_avg;
79              ski_data_fischer812_1{2,measurement} =
                    w_profile;
80              ski_data_fischer812_1{3,measurement} =
                    w_left_avg;
81              ski_data_fischer812_1{4,measurement} =
                    w_right_avg;
82              ski_data_fischer812_1{5,measurement} =
                    w_total;
83          elseif ski == 2
84              ski_data_fischer812_2{1,measurement} =
                    w_profile_avg;
85              ski_data_fischer812_2{2,measurement} =
                    w_profile;
86              ski_data_fischer812_2{3,measurement} =
                    w_left_avg;
87              ski_data_fischer812_2{4,measurement} =
                    w_right_avg;
88              ski_data_fischer812_2{5,measurement} =
```

```
                w_total;
89          elseif ski == 3
90              ski_data_fischer902_1{1,measurement} =
                    w_profile_avg;
91              ski_data_fischer902_1{2,measurement} =
                    w_profile;
92              ski_data_fischer902_1{3,measurement} =
                    w_left_avg;
93              ski_data_fischer902_1{4,measurement} =
                    w_right_avg;
94              ski_data_fischer902_1{5,measurement} =
                    w_total;
95          elseif ski == 4
96              ski_data_fischer902_2{1,measurement} =
                    w_profile_avg;
97              ski_data_fischer902_2{2,measurement} =
                    w_profile;
98              ski_data_fischer902_2{3,measurement} =
                    w_left_avg;
99              ski_data_fischer902_2{4,measurement} =
                    w_right_avg;
100             ski_data_fischer902_2{5,measurement} =
                    w_total;
101         end
102     end
103 end
104 % Saving data
105 ski_data_0107{1,3} = ski_data_fischer812_1;
106 ski_data_0107{2,3} = ski_data_fischer812_2;
107 ski_data_0107{3,3} = ski_data_fischer902_1;
108 ski_data_0107{4,3} = ski_data_fischer902_2;
109 %%
110 w_left_avg = mean(w_left, 1);
111 w_right_avg = mean(w_right, 1);
112 w_left_avg(w_left_avg<-200) = 0;
113 w_right_avg(w_right_avg<-200) = 0;
114 w_profile = [w_right_avg;w_left_avg];
115 w_profile_avg = mean(w_profile,1);
116 % 2D-plots
117 figure();
118 subplot(2,2,1);
```

```
119 title('Left channel');
120 ylabel('Weight [g]');
121 xlabel('Sensor location [mm]');
122 hold all;
123 plot(x_axis_sensor_location, w_left_avg, 'b');
124 plot(x_axis_sensor_location, w_left_avg, 'or');
125 ylim([-1000,12000]);
126 grid on;
127
128 subplot(2,2,2);
129 title('Right channel');
130 ylabel('Weight [g]');
131 xlabel('Sensor location [mm]');
132 hold all;
133 plot(x_axis_sensor_location, w_right_avg, 'b');
134 plot(x_axis_sensor_location, w_right_avg, 'or');
135 ylim([-1000,12000]);
136 grid on;
137
138 subplot(2,2,[3 4]);
139 title('Both channels');
140 ylabel('Weight [g]');
141 xlabel('Sensor location [mm]');
142 hold all;
143 plot(x_axis_sensor_location, w_left_avg, 'b');
144 plot(x_axis_sensor_location, w_right_avg, 'r');
145 plot(x_axis_sensor_location, w_profile_avg, 'g','
    LineWidth',2);
146 legend('Left channel','Right channel', 'Channel average
    ')
147 ylim([-1000,12000]);
148 grid on;
149 suptitle('Fischer SPEED MAX Classic Plus 812 #2 [40Kg]'
    );
150 %suptitle('Subplot Grid Title','Color','red');
151 w_total = (sum(w_left_avg) + sum(w_right_avg))/1000;
152 %% Saving the data
153 save('data/31mai')
154 filename = 'data/31mai-calibration-test';
155 xlswrite(filename,profile);
```